Li et al. *Microsystems & Nanoengineering* (2026)12:133
https://doi.org/10.1038/s41378-026-01159-7

Microsystems & Nanoengineering
www.nature.com/micronano

ARTICLE Open Access

Theoretical modelling and optimization design of PMUT arrays for enhanced acoustic performance

Zixuan Li[1,2], Dejiang Lu[1,3,4]✉, Zhikang Li[1,3,4], Hongqiang Tan[1,4], Jiawei Yuan[1,2], Zilong Zhao[1,2], Yihe Zhao[1,3,4], Zimeng Zhang[1,4], Shaohui Qin[1,4], Xiaozhang Wang[1,4], Min Li[1,3,4], Kui Zhang[5], Ran Dong[5], Libo Zhao[1,3,4]✉ and Lihong Fan[6]✉

Abstract

Theoretical models are essential for performance analysis and structure optimization design of large-scale piezoelectric micromachined ultrasonic transducers (PMUT) arrays. However, current models have rarely incorporated the inter-element crosstalk and oversimplified the electro-mechanical-acoustic coupling, leading serious discrepancies with experimental results and limiting the array optimization design and performance improvement. To address this, a novel electro-mechanical-acoustic coupling model and a spatial acoustic field modeling approach are proposed for PMUT arrays, incorporating distributed deformation functions of individual element and mutual acoustic impedance to analyse key performance metrics such as transmission power, frequency response, focal length, and beamwidth. Its accuracy is validated through finite element simulations, demonstrating small deviations of less than 3%. Parametric studies reveal that increasing the filling ratio from 20% to 60% improves transmission power and bandwidth but significantly increases crosstalk, reducing focusing efficiency. Enlarging the array size results in proportional increases in acoustic output power and focal pressure, while simultaneously reducing beamwidth, thereby improving directivity. As for array arrangements, circular array achieves higher focal pressure than square array, albeit with shorter focal lengths. Annular array, with its distinct mainlobe and ring-shaped sidelobes, demonstrates superior focal pressure at longer distances, ideal for extended-range applications. The theoretical models are further validated by experimental results from fabricated square, hexagonal, circular, and annular PMUT arrays. This study proposes an accurate theoretical model for PMUT arrays, enabling accurate and reliable prediction of key acoustic performance metrics in large-scale arrays, and facilitating the array structure optimization design and performance enhancement of PMUT.

Introduction

Piezoelectric micromachined ultrasonic transducers (PMUT)[1] exhibited great potential in developing next-generation ultrasonic medical imaging, non-destructive testing, and consumer electronics technologies[2,3], owing to their distinct advantages over traditional bulk piezoelectric transducers[4], such as miniaturized volume, improved acoustics impedance matching with human tissue and fluid, and ease integration with integrated circuits[5]. PMUT operate in the d_{31} flexural vibration mode[6], exhibiting lower acoustic impedance than conventional d_{33} thickness-mode transducers[7], making them ideal for portable and consumer electronics[8]. Compared to capacitive micromachined ultrasonic transducers (CMUTs)[9], PMUT do not require high DC bias voltages, simplifying fabrication and enhancing design flexibility[10]. Their sub-wavelength feature size allows individual elements to act as point sources[11], enabling beamforming with controllable focal length, beamwidth, and acoustic output[12]. PMUT are increasingly used in applications such as biomedical imaging, non-destructive testing, and underwater

---

Correspondence: Dejiang Lu (djlu@mail.xjtu.edu.cn) or
Libo Zhao (libozhao@xjtu.edu.cn) or
Lihong Fan (lhfan@xjtu.edu.cn)
[1]State Key Laboratory for Manufacturing System Engineering, State Industry-Education Integration Center for Medical Innovations, International Joint Laboratory for Micro/Nano Manufacturing and Measurement Technologies, Shaanxi Innovation Center for Special Sensing and Testing Technology in Extreme Environments, Shaanxi Provincial University Engineering Research Center for Micro/Nano Acoustic Devices and Intelligent Systems, Xi'an Jiaotong University, Xi'an, China
[2]School of Mechanical Engineering, Xi'an Jiaotong University, Xi'an, China
Full list of author information is available at the end of the article

sensing, where high-resolution, large-scale arrays are crucial for improved performance.

Despite aforementioned progress in PMUT technologies, several of their main performances, such as the transmitting acoustic pressure, receiving sensitivities and bandwidth, still cannot meet the requirements of practical applications. For this, a large number of researchers devoted their efforts on structure design and optimization. For example, Gong et al.[13] introduced a coupled cantilever dual-cavity PMUT with a bimorph configuration, enhancing sensitivity by 48% and reducing frequency variation to under 2%. Wang et al.[14] developed serial dual-cavity PMUT with Helmholtz resonators for dual-band operation, achieving a 32% bandwidth increase. On the materials side, Li et al.[15] introduced magnetron-sputtered PZT thin film for PMUT fabrication, achieving the piezoelectric coefficient of 15.5 pC/m^2, a 30% improvement over sol-gel derived thick films. Zhao et al.[16] explored eco-friendly KNN-based lead-free PMUT, achieving a −6 dB bandwidth of 95.7% and a transmitting sensitivity of 3.8 kPa/V, comparable to traditional PZT devices. In the development of PMUT modeling techniques, the equivalent circuit model (ECM) has emerged as an efficient alternative to finite element analysis for rapid performance prediction and design iteration[17]. Early ECM approaches primarily focused on single-element transducers, employing analogies between mechanical, electrical, and acoustic domains to simulate device behavior. For instance. Smyth et al.[18] established an analytical Mason equivalent circuit for a single circular PMUT element, providing a foundation for basic resonance and impedance analysis. Wang et al. developed a theoretical model of ScAlN-based PMUT element under different DC biases[19]. Although PMUT cell structure design can significantly contribute to performances enhancement, yet their performances still prominently influenced by the array parameters, such as filling ratio, array size and configuration. For instance, the key performance metrics, including bandwidth, sensitivity, directivity, acoustic pressure, and spatial resolution, are dictated by these array design parameters[20]. The relationship between an individual PMUT element and the overall array is critical for accurately predicting the array's electro-acoustic performance[21]. Due to the small inter-element spacing and high element density, the vibration of each element is influenced not only by its own excitation but also by the radiated acoustic field from neighboring elements, which can alter both its amplitude and phase. To account for these interactions, the array-level model incorporates mutual radiation impedance, coupling all elements through a complex impedance matrix. This formulation effectively integrates single-element behavior into the array response, ensuring that inter-element acoustic interactions are fully represented. Conventional array configurations may lead to severe acoustic crosstalk and inhomogeneous acoustic pressure, degrading these performances[22]. Therefore, it is essential to investigate the influence of PMUT array parameters on these performance before structure optimization design. For a 20 × 20 PMUT array, a complete frequency-domain finite element method (FEM) simulation requires over 10 h of computation using a dual-processor setup (Intel® Xeon® Gold 5218, 16-core ×2)[23]. The ECM, in particular, has been widely adopted for its computational efficiency in simulating the electro-mechanical-acoustic behavior of PMUT. While Zhao et al.[23] developed an ECM to analyze the performance of small PMUT arrays for bandwidth optimization, without incorporating the vibration theory model of the individual element. Abdalla et al.[24] introduced a numerical reduced-order technique for complex multi-layered PMUT arrays, significantly reducing computational costs. However, the theoretical modeling and design of large-scale PMUT arrays, considering the element vibration and mutual radiation acoustic impedance, have been rarely developed. Additionally, the FEM faced high computational costs when applied to large arrays, limiting their practical application in iterative design optimization of large-scale PMUT array[24].

Equivalent circuit model had been widely applied to describe the electromechanical–acoustic coupling of piezoelectric devices, from early Mason and KLM models[25] to more recent adaptations for PMUT. While these approaches improved the prediction of single-element performance, they generally neglected array-level mutual coupling and acoustic interactions. To overcome this limitation, this work developed a novel comprehensive electro-mechanical-acoustic coupling model for PMUT arrays, enabling efficient and accurate performance prediction of large-scale PMUT arrays. The electro-mechanical domain of the piezoelectric thin film was developed based on plate-shell vibration theory, with the acoustic domain based on the membrane's vibration as the boundary condition. A force-electricity analogy was employed to couple the electromechanical and acoustic domains, resulting in the ECM model for a single PMUT element. By introducing mutual radiation acoustic impedance, the ECM for PMUT arrays was derived. Furthermore, a quantitative analysis was conducted to predict the key performance metrics of PMUT, such as transmission power, acoustic pressure, beamwidth, and focal length. Compared with conventional finite element methods, the proposed method significantly enhanced computational efficiency while maintaining high accuracy, with FEM validation showing deviations below 3%. Experimental results from four PMUT arrays (70 μm radius, 40 μm pitch) confirmed the model's predictive capability, with measured resonant frequencies in air and water closely matching the theoretical results (deviations below 5%).

Parametric studies demonstrated that increased array size improved output power and focusing area, while reduced spacing enhances bandwidth but may introduce crosstalk and suppress output power. Among different array arrangements, square array exhibited a long focal length, while circular arrays had a short focal distance but generate high output acoustic pressure. Ring array was characterized by prominent mainlobe and ring-shaped sidelobe, capable of focusing acoustic fields at greater distances. In conclusion, this work provides a parameter optimization framework for the performance analysis of the PMUT arrays, facilitating their practical application in biomedical imaging, underwater sensing, and nondestructive testing.

Materials and method

Theoretical modeling of PMUT array

Equivalent circuit models have widely considered as an effective approach to analyze the performances of PMUT arrays composed of hundreds of cells. To establish the ECM of PMUT array, we first modeled the electromechanical and acoustic domains of a circular PMUT element based on plate-shell vibration theory[26] and the acoustic emission model[25]. An electro-mechanical-acoustic equivalent circuit is then constructed using an analog method based on the derived domain parameters. To quantify acoustic crosstalk (Fig. 1a), the mutual radiation impedance was incorporated into the equivalent circuit, thereby establishing a comprehensive ECM for PMUT arrays. The relationship between element distribution, crosstalk characteristics, and output sensitivity within the array was subsequently analyzed. Based on the developed model, analytical expressions for key performance metrics of the PMUT array were derived and later validated through FEM simulations presented in the following sections.

The vibrating area of the composite film is shown in Fig. 1b. The PMUT membrane has a radius r_c, with its edge fully clamped, while the bottom electrode has a radius r_e. The Young's modulus, thickness, density, and Poisson's ratio of the material in the ith layer are denoted as Y_i, h_i, ρ_i, and ν_i, respectively. The PMUT operates in the d_{31} flexural vibration mode, where the alternating electric field E_p applied to the piezoelectric layer generates a transverse stress σ_p at a distance Z_p from the neutral plane z_n. The stress induces a bending moment M_p, which leads to the bending deformation of the film. Based on the Eqs. (A1) and (A2) in Appendix A, the bending moment M_p can be further given as:

$$M_p = e_{31,f} V_{in} Z_p \tag{1}$$

$$Z_p = h_1 + \frac{h_2}{2} - z_n \tag{2}$$

Since the thickness of the electrode and insulating layers is typically 100–200 nm, much smaller than that of the piezoelectric and structural layers, the PMUT composite film can be approximated as a two-layer structure (piezoelectric and structure layers). Compared with the complete multilayer PMUT model, the two-layer (PZT/Si) simplification can reduce 3D FEM simulation time from 3 h 47 min to 37 min, while introducing only a 2.2% shift in the resonance frequency and 3.1% error in acoustic power (Fig. 2f). Furthermore, this simplification significantly will improve the computational efficiency of array-level simulations, thus facilitating the investigation of performance variations in PMUT arrays. In subsequent theoretical modeling based on the actual fabrication parameters of each thin film, a correction factor K for the neutral plane thickness will be firstly introduced by considering the material properties and thicknesses of the multilayer composite stack, thereby further improving the modeling accuracy and efficiency. Accordingly, the neutral plane z_n can be defined as:

$$z_n = \sum_{i=1}^{2} \frac{Y_i\left(z_i^2 - z_{i-1}^2\right)}{1-\nu_i^2} \Big/ \frac{Y_i h_i}{1-\nu_i^2} + K \tag{3}$$

For the circular vibration plate excited by an alternating voltage source with the angular frequency $\omega = 2\pi f$, the governing vibration equation[27] under the piezoelectric moment M_p and incident pressure P_{res} can be given as:

$$D\nabla^2\nabla^2 w + \rho_s \frac{\partial^2 w}{\partial^2 t} = P_{res} + \nabla^2 M_p \tag{4}$$

Where D and ρ_s are the flexural rigidity and surface density of the composite membrane, and can be defined as:

$$D = \sum_{i=1}^{2} \frac{Y_i}{1-\nu_i^2}\left(\frac{h_i^3}{12} + z_i^2 h_i\right) \tag{5}$$

$$\rho_s = \sum_{i=1}^{2} \rho_i h_i \tag{6}$$

The general solution to Eq. (4) is expressed as:

$$w(r,\theta,t) = W(r,\theta)e^{j\omega t} \tag{7}$$

Based on the thin-film deformation solution Eq. (A15) derived from Dirac's functional integration theorem[28,29], the plate-shell deformation equations $W_p(\mathrm{r})$ and $W_m(\mathrm{r})$,

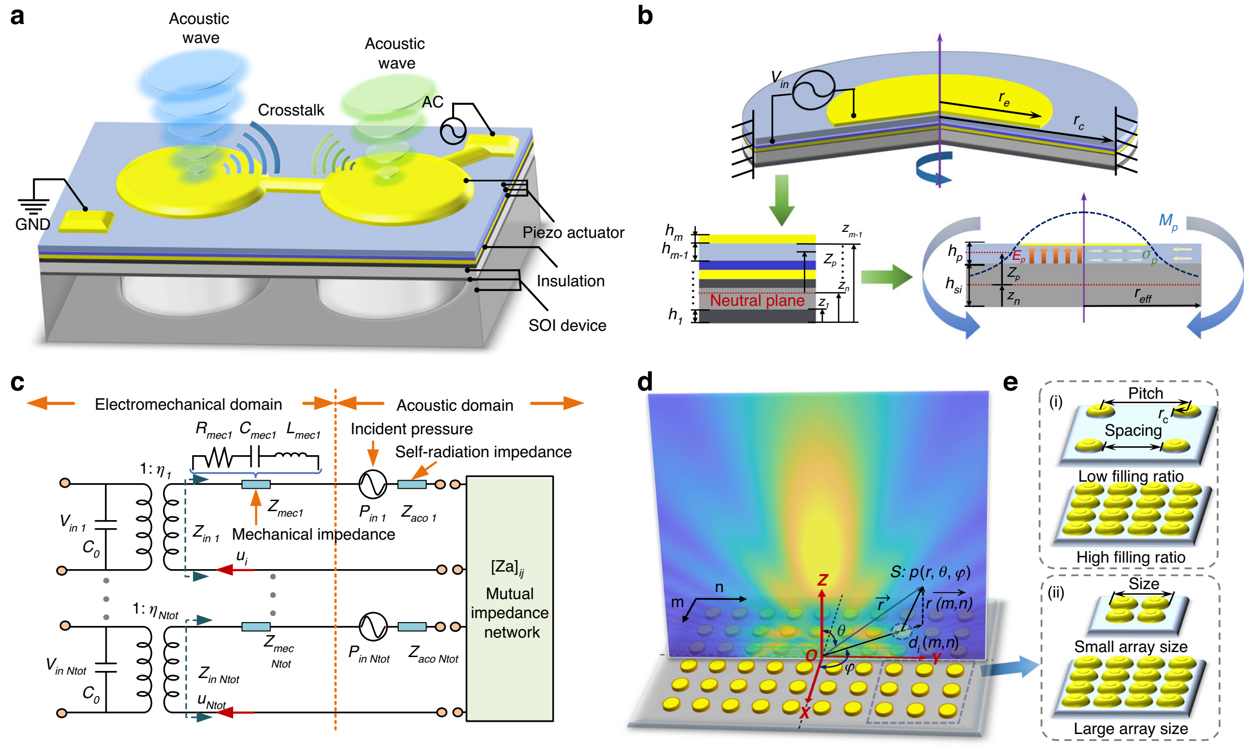

Fig. 1 PMUT theoretical analysis model. a Structure schematic of a PMUT cell. **b** Simplified mechanical schematic of a PMUT cell. **c** Equivalent circuit model of a PMUT array. **d** 3-D schematic of a PMUT array. **e** Structural parameter variations in the PMUT array: (i) Variation in filling ratio; (ii) Variation in array size

caused by the pressure load P_{res} and the piezoelectric driving moment M_p, can be expressed as:

$$W_p(r) = \frac{P_{res} r_c^2}{\pi D} \sum_{i=1}^{\infty} \frac{\left[\frac{J_1(\pi\beta_i)}{\beta_i} - \frac{J_0(\pi\beta_i)}{\beta_i I_0(\pi\beta_i)} I_1(\pi\beta_i) \right]}{\Lambda_i \left[\left(\frac{\pi\beta_i}{r_{c0}} \right)^4 - \beta^4 \right]} \psi_i(r) \tag{8}$$

$$W_m(r) = \frac{\pi}{r_c D} \sum_{i=1}^{\infty} \frac{M_p \left[-r_e \left[\beta_i J_1\left(\frac{\pi\beta_i}{r_c} r_e \right) + \beta_i \frac{J_0(\pi\beta_i)}{I_0(\pi\beta_i)} I_1\left(\frac{\pi\beta_i}{r_c} r_e \right) \right] \right]}{\Lambda_i \left[\left(\frac{\pi\beta_i}{r_{c0}} \right)^4 - \beta^4 \right]} \psi_i(r) \tag{9}$$

Thus, the volumetric displacement excited by the incident pressure Y_m and the electromechanical admittance b_t can be expressed as:

$$Y_m = \int_0^a 2\pi r \cdot \frac{W_p(r)dr}{P_{res}} \tag{10}$$

$$b_t = \int_0^a 2\pi r \cdot \frac{W_m(r)dr}{V_{in}} \tag{11}$$

Building on the analytical vibration model of a single PMUT element derived from the aforementioned mechanical analysis, the ECM is developed to evaluate PMUT array performance. The model incorporates volumetric displacement and electromechanical admittance expressions via mechanical–electrical–acoustic analogies. With PMUT elements connected in parallel to form array, the ECM enables efficient analysis of key performance metrics by mapping all mechanical and acoustic parameters to their electrical counterparts. The schematic of the ECM is shown in Fig. 1c. C_0 is the feedthrough capacitance, V_{in} is the input voltage, and P_{in} is the incident acoustic pressure on the surface of the PMUT membrane. The mechanical impedance Z_{mec} consists of the equivalent resistance R_{mec} (representing damping through acoustic impedance), the equivalent capacitance C_{mec} (representing stiffness), and the equivalent inductor L_{mec} respectively (representing additional fluid mass). Z_{aco} is the self-radiation impedance of the PMUT element; η is the electro-mechanical transduction

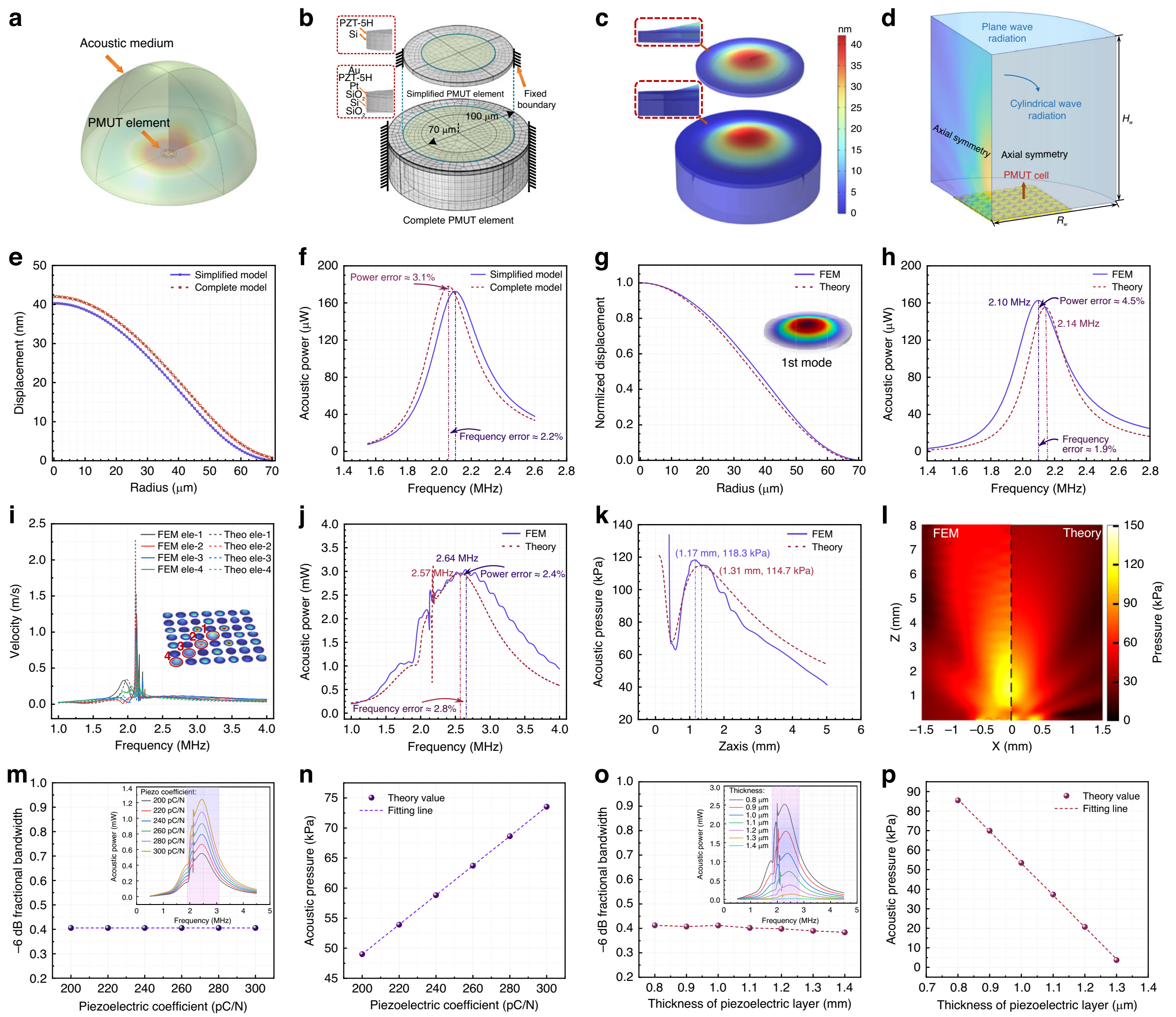

Fig. 2 FEM validation and analytical verification of the ECM for single PMUT element and array performance. a 3D FEM model of a PMUT cell. **b** Schematics of the electro-mechanical domain of a simplified thin-film PMUT model and a complete multilayer PMUT model. **c** Comparison of vibration modes and displacement distributions between the simplified and the complete model. **d** 1/4-axisymmetric FEM model of a 7 × 7 PMUT array. **e** Cross-sectional displacement profiles of the simplified and complete models. **f** Frequency response comparison of the simplified and complete models. **g** Comparison of normalized displacement between FEM and ECM results for the simplified model. **h** Frequency response of the simplified model with the acoustic power. **i** Vibration velocity distribution of array elements along the diagonal. **j** Frequency response of the PMUT array with the acoustic power. **k** Acoustic pressure in the central axis of the PMUT array. **l** Acoustic field distribution in the central XOZ plane of the array. **m**–**n** Influence of piezoelectric coefficient variation on the bandwidth and the acoustic pressure of the PMUT array (**o**) and (**p**) Influence of piezoelectric layer thickness variation on the bandwidth and the acoustic pressure of the PMUT array

ratio. The expressions of C_0, Z_{mec}, Z_{aco}, and η can be presented in Appendix B. u represents the velocity of the membrane, while $[Z_{aij}]$ is an $N_{\mathrm{tot}}\times N_{\mathrm{tot}}$ mutual radiation impedance matrix that describes the mutual acoustic interaction between cells i (x_i, y_i) at and j (x_j, y_j) in the PMUT array[21], as shown in Fig. 1d. Here, $N_{\mathrm{tot}} = m\times n$ represents the total number of PMUT cells.

The vibration of the entire circular region is equivalent to that of a vibrating piston with an effective radius of r_{eff}. In this case, the self-radiating impedance Z_{self} can be simplified by Eq. (B5) as:

$$Z_{\mathrm{self}} = \rho c\pi r_{eff}^2\left[1-\frac{J_1(2kr_{\mathrm{eff}})}{kr_{eff}}+j\cdot\frac{4}{\pi}\int_0^{\frac{\pi}{2}}\sin(2kr_{eff}\cos(x))\sin^2(x)dx\right] \tag{12}$$

Considering that the planar feature size of the PMUT cell is much smaller than the acoustic wavelength in the medium, any PMUT element with a single circumferential constraint can be acoustically equivalent to a circular piston vibration, regardless of its planar shape. The acoustic field distribution produced by the circular vibrating piston[25] is given by:

$$p_{\mathrm{cir}i} = j2\rho c v_{\mathrm{cir}i} \sin\left|\frac{k\left(\sqrt{d^2 + r_{\mathrm{eff}}^2} - d\right)}{2}\right| e^{j(\omega t - kd - \xi)} \cdot D_{\mathrm{cir}}(\theta) \tag{13}$$

$$\xi = \frac{k\left(\sqrt{d^2 + r_{\mathrm{eff}}^2} - d\right)}{2} \tag{14}$$

$$D_{\mathrm{cir}}(\theta) = \frac{2J_1(kr_{\mathrm{eff}} \sin\theta)}{kr_{\mathrm{eff}} \sin\theta} \tag{15}$$

Where $v_{\mathrm{cir}\ i}$ equals to $u_i/(\pi r_{\mathrm{eff}}{}^2)$; u_i represents the volumetric velocity of the membrane vibration for each PMUT element in the array, which can be determined using Kirchhoff's voltage law and the ECM shown in Fig. 1c. This can be expressed as:

$$u_i = \frac{\eta V_{in}}{Z_{\mathrm{in}i}} \tag{16}$$

Where $Z_{\mathrm{in}\ i}$ represents the total impedance of the vibration element. As shown in Fig. 1c, the input impedance $Z_{\mathrm{in}\ i}$ of each element in the array is the sum of the mechanical impedance $Z_{\mathrm{mec}\ i}$, the self-radiation impedance $Z_{\mathrm{self}\ i}$, and the mutual radiation impedance $\Sigma Z_{\mathrm{a}\ ij}$, which can be given as:

$$Z_{\mathrm{in}i} = Z_{\mathrm{mec}i} + Z_{\mathrm{aco}ii} + \sum_{\substack{j=1 \\ i\neq j}}^{N_{tot}} \frac{u_j}{u_i} Z_{\mathrm{a}ij} = Z_{\mathrm{mec}i} + + \sum_{j=1}^{N_{tot}} \frac{u_j}{u_i} Z_{ij} \tag{17}$$

Where:

$$Z_{ij} = \begin{cases} Z_{\mathrm{aco}ii}\ i = j \\ Z_{\mathrm{a}ij}\ i \neq j \end{cases} \tag{18}$$

The mutual radiation acoustic impedance $Z_{\mathrm{a}\ ij}$ between different PMUT cell i and cell j can also be expressed as the interaction between two equivalent circular pistons, which can be described as:

$$z_{\mathrm{a}ij} = \frac{1}{\pi r_{\mathrm{eff}}^2}\left[\rho c \cdot \frac{(kd_{ij})^2}{2}\right] \cdot \left[\frac{\sin(kd_{ij})}{kd_{ij}} + j \cdot \frac{\cos(kd_{ij})}{kd_{ij}}\right] \tag{19}$$

Where d_{ij} is the distance between the centers of two PMUT cells, i and j, which can be expressed as:

$$d_{ij} = \sqrt{(x_i - x_j)^2 + (y_i - y_j)^2} \tag{20}$$

The transmission power of an individual PMUT element is calculated by multiplying the real input impedance $Z_{\mathrm{in}\ i}$ with its volumetric velocity u_i. The total transmission power of the PMUT array (W_{tot}) is calculated by summing the acoustic radiation power by each element within the array. To evaluate the acoustic transmission capabilities of different PMUT arrays, the transmission power per unit voltage W_{tot} is defined as follow:

$$W_{tot} = \sum_{j=1}^{N_{tot}} \frac{\frac{1}{2} real(Z_{\mathrm{in}i})|u_i|^2}{V_{in}} \tag{21}$$

The bandwidth determines the PMUT frequency response range and imaging resolution. The −6 dB fractional bandwidth (*FBW*) of PMUT array can be expressed as:

$$FBW = \frac{f_h - f_l}{f_c} \times 100\% \tag{22}$$

Where f_h and f_l are the frequencies corresponding to half of the maximum amplitude on the rising and falling sides, respectively, while f_c is the frequency corresponding to the maximum amplitude.

Figure 1d depicted the cell distribution in the PMUT array, where the PMUT element at position (m, n) is located in the m-th row and n-th column. The position vector $d_i\ (m, n)$ represents the location of element (m, n) relative to the center of the array, while vector r refers to the spatial coordinates (r, θ, ϕ) relative to the array center, and $r_i\ (m, n)$ denotes the position vector of a point (r, θ, ϕ) in the medium, relative to the PMUT element at (m, n):

$$\begin{aligned} \vec{r}_i(m,n) = {} & [r\sin(\theta)\cos(\phi) - (m - m_0)\Delta x]\vec{e}_x \\ & + + [r\sin(\theta)\sin(\phi) - (n - n_0)\Delta y]\vec{e}_y + r\cos(\theta)\vec{e}_z \end{aligned} \tag{23}$$

Table 1 The parameters used for the modeling of PMUT

Symbol	Parameters	Value	Unit
r_c	Diaphragm radius	70	μm
r_e	Top electrode radius	46.9	μm
h_1	Thickness of structure layer (Si)	5	μm
h_2	Thickness of piezoelectric layer (PZT)	1	μm
E_1	Young's modulus of Si	170	GPa
E_2	Young's modulus of PZT	190	GPa
v_1	Poisson's ratio of Si	0.28	/
v_2	Poisson's ratio of PZT	0.34	/
d_{31}	Piezoelectric coefficient of PZT	274	pC/N
ε_0	Relative dielectric constant of PZT	900	/
N	Cell number	49	/
Spa	Cell spacing	40	μm
R_0	Acoustic domain radius of PMUT cell	0.5	mm
R_w	Acoustic domain radius of PMUT array	1.5	mm
H_w	Acoustic domain height	8	mm
c_0	Fluid (water) sound velocity	1500	m/s
ρ_0	Fluid (water) density	1000	kg/m^3
V_{in}	Input Voltage	1	V

Consequently, based on Eq. (22), the acoustic pressure at any point in space can be expressed as:

$$P(r,\theta,\phi)=\sum_{n=1}^{N}\sum_{m=1}^{M}p_{\mathrm{ciri}}(m,n)=\sum_{n=1}^{N}\sum_{m=1}^{M}\left(\frac{j\rho cku_i}{2\pi}Dir(\theta,\phi)\frac{e^{-jkr_i(m,n)}}{r_i(m,n)}\right) \tag{24}$$

Validation of theoretical models with FEM

The theoretical model for the PMUT element was established based on its vibrational displacement and self-radiating acoustic impedance, with its accuracy verified through FEM simulations using COMSOL Multiphysics. The geometric and material parameters of the vibrating membrane were listed in Table 1. As shown in Fig. 2a, a 3D FEM model of the PMUT cell[30] was constructed, consisting of both acoustic and electro-mechanical domains. The pressure acoustics module simulated the operating environment (e.g., water), with the acoustic medium modeled as a hemispherical region with a radius R_0, and its boundary set as a spherical wave radiator. Radiated acoustic power was computed by integrating the acoustic pressure over this surface. Figure 2a presented both a simplified thin-film PMUT model and a complete multilayer PMUT model. The simplified model consisted of a 1 μm-thick PZT layer and a 5 μm-thick silicon structural layer. In contrast, the complete model incorporated additional layers: a 100 nm Au top electrode, a 1 μm PZT layer, a 100 nm Pt layer, a 200 nm SiO_2 layer, a 5 μm silicon structural layer, and a 100 μm silicon substrate. For boundary conditions, the simplified model employed a clamped edge at the periphery of the 70 μm-radius vibrating region. The complete model, however, used a fixed support applied at a radial distance of 100 μm to better approximate realistic constraints. Identical meshing schemes were adopted within the active region in both models to ensure consistency. The interface between the vibrating membrane and the acoustic medium was defined as a sound-solid coupling boundary. The membrane edge was fully clamped, with an excitation voltage V_{in} applied between the top and bottom electrodes. Figure 2c revealed that both the simplified and complete models exhibited similar vibration modes and displacement distributions. The cross-sectional displacement profiles in Fig. 2e indicated a deviation of approximately 2 nm, resulting from the lower neutral-plane position of the multilayer diaphragm compared to the simplified model. This observed discrepancy provided the foundation for introducing a neutral-plane compensation factor, K, in subsequent theoretical modeling. Furthermore, the frequency response curves in Fig. 2f showed a 2.2% shift in resonant frequency and a 3.1% variation in acoustic output power between the two models. Furthermore, a comparison between the theoretical predictions and FEM results was shown in Fig. 2g–h. The normalized displacement obtained from the FEM simulation demonstrated excellent agreement with the ECM, as illustrated in Fig. 2g. The resonant frequency of the PMUT cell was approximately 2.1 MHz, with a relative error of around 1.9%, as presented in Fig. 2h, confirming the computational accuracy of the theoretical model.

A FEM simulation model for PMUT arrays was further established to validate the theoretical calculation results based on the ECM. As shown in Fig. 2d a 1/4-axisymmetric FEM simulation was employed to enhance computational efficiency[31,32]. The simulation domain consisted of a quarter-cylinder with a radius R_w of 1.5 mm and a height H_w of 8 mm. The electromechanical coupling area of the PMUT array was modeled using solid mechanics and electrostatic modules, incorporating a 7 × 7 array of circular membranes within a water-filled cylinder. The material and structural parameters used in the FEM and ECM were summarized in Table 1. The validation of the FEM model parameters has been provided in the Supplementary Materials. The simulation of the PMUT array employed a mesh size of 200 μm and a frequency step of 5 kHz, utilizing a spherical wave radiation (SWR) boundary condition to ensure computational accuracy. The Multiphysics field setup followed the steps previously described. Frequency domain

Table 2 The parameters comparison between FEM and Theory

Method	Array	Computation time	Frequency deviation	Scalability
FEM This work	1 × 1	37 min	/	Element
	7 × 7	85 h 10 min	/	Small array
ECM This work	1 × 1	0.63 s	2.2%	Element
	7 × 7	4.2 s	2.8%	Multiple arrays
ECM[44].	1 × 1	/	3%	Element
ECM[23].	3 × 3	/	5.5%	Square array
ECM[45].	3 × 3	/	7%	Square array

analysis was performed to evaluate the acoustic transmission power, acoustic field, and axial acoustic pressure. Transmission power was computed by integrating the acoustic field at the boundary of the acoustic operating cylinder. Axial acoustic pressure was determined by calculating the absolute pressure at the resonant frequency. Figure 2i–l presented the comparison results between theoretical calculations and FEM simulations for the main performance of the studied PMUT array. As shown in Fig. 2i, the vibration velocities of the PMUT array elements along the diagonal exhibited good agreement between the FEM simulations and theoretical predictions, with average errors of only 4% in amplitude and 3% in phase. The corresponding velocity and phase distributions for all array elements were provided in Supplementary Figs. S9–S11 and Supplementary Video. Figure 2j displayed the frequency response in terms of transmitted power, revealing a strong consistency between the FEM results and theoretical predictions, which confirmed that Eq. (21) accurately described the acoustic power behavior of the PMUT array. The phase inconsistency among PMUT array elements, with some vibrating in positive phase and others in negative phase, generated alternating regions of positive and negative sound pressure in the acoustic field, forming a distinct interference pattern (Fig. S14a). To analyze the sound field in the central XOZ plane of the array at 2.6 MHz, the sound pressure generated in the surrounding fluid domain was computed, and the pressure distribution along the central axis was extracted. The point of maximum pressure along this axis was identified as the acoustic focus, with the corresponding value defined as the focal pressure. To mitigate the influence of interference oscillations on quantitative analysis, an envelope-based midline smoothing method was applied to the original fluctuating curve (Fig. S14c–d). The smoothed FEM axial sound pressure distribution was then compared with the theoretical model results, revealing strong consistency, as shown in Fig. 2k. The sound pressure distribution from the FEM results correlated well with the ECM calculations using Eq. (24). The deviation for all performance parameters remained below 3%, affirming the effectiveness and accuracy of the developed analytical expressions in characterizing the key properties of PMUT arrays. To further quantify the influence of deviations in the piezoelectric coefficient and fabrication-induced variations in the piezoelectric layer thickness on device performance, simulations were conducted on a 7 × 7 square PMUT array. As shown in Fig. 2m–p, key acoustic performance metrics, including bandwidth and sound pressure, were evaluated. The results indicated that variations in the piezoelectric coefficient and layer thickness had negligible impact on the resonant frequency and bandwidth (Fig. 2m, o). In contrast, the output sound pressure exhibited a linear positive correlation with the piezoelectric coefficient, whereas an inverse linear relationship was observed with the piezoelectric layer thickness (Fig. 2n, p). These systematic correlations provide valuable guidance for refining theoretical models and improving the predictive accuracy of PMUT array performance in fabricated devices.

In addition, a comprehensive comparison of different ECMs for PMUT arrays analysis was presented in Table 2. The proposed model was shown to demonstrate superior accuracy and scalability while maintaining competitive computational efficiency, which rendered it highly suitable for the simulation and optimization of large-scale PMUT arrays. Furthermore, a subsequent parametric investigation was conducted to examine the influence of structural parameters on the main performances of PMUT array, such as the array filling ratio, array size, and array arrangement. The array filling ratio, defined as the ratio of the total region occupied by all elements to the total array size, significantly influenced the crosstalk between cells, as shown in Fig. 1e-i. The array size, representing the total dimension of the array, had a direct impact on both the transmitted acoustic power and the spatial distribution of the acoustic field, as shown in Fig. 1e-ii. Additionally, the element arrangement played a critical role in shaping the acoustic beam directivity. All ECM calculations were performed using consistent material and structural parameters for PMUT FEM simulations, as specified in Table 1.

The effect of array filling ratio on the performance of PMUT

In this section, the effect of filling ratio of the PMUT array on its performance was first quantified using the established analytical expressions. As illustrated in Fig. 3a, with a fixed array size of 2 × 2 mm and an element radius

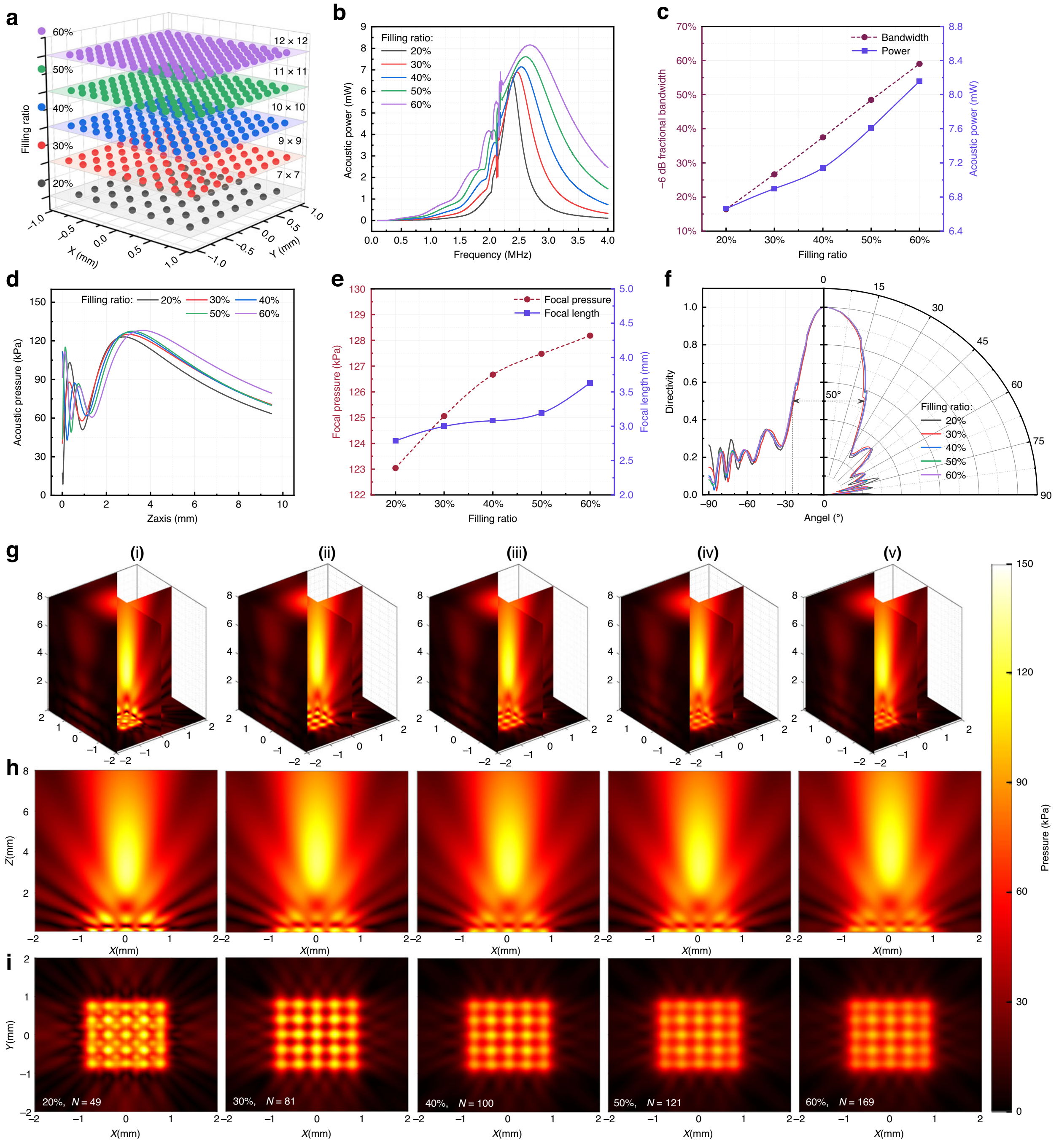

Fig. 3 The effect of filling ratio on the acoustic performance of PMUT arrays. a Schematic of PMUT array with the filling ratio ranging from 20% to 60%. **b** The frequency response of acoustic power. **c** Variations in the -6 dB fractional bandwidth and acoustic output power. **d** Transmitting acoustic pressure along the central axis of the PMUT array. **e** Variations in the focal pressure and length. **f** The directivity of the acoustic beam. **g** Cross-sectional view of the theoretical 3D spatial sound pressure distribution of PMUT arrays in a $4 \times 4 \times 8\ \mathrm{mm}^3$ area. **h** Acoustic pressure distribution in the central X-Z plane. **i** Acoustic pressure distribution in the X-Y plane (Z = 1 mm)

of 70 μm, the filling ratio was varied from 20% to 60%, corresponding to 49, 81, 100, 121, and 169 cells, respectively. The investigated range of filling ratios was reasonable, as it encompassed the typical variation observed in PMUT arrays[33,34]. Figure 3b presented the variation of acoustic power of the PMUT array with respect to the filling ratio across 0–4 MHz, showing that increased filling ratio intensified acoustic crosstalk between adjacent cells.

Additionally, the resonant frequency exhibited a shift from 2.3 MHz to 2.7 MHz with increased filling ratio. As shown in Fig. 3c, the transmitting power increased from 6.65 mW to 8.15 mW as the filling ratio rose from 20% to 60%. A similar trend was observed for the bandwidth, which expanded from 16.4% to 59% over the same range. Figure 3d showed the axial acoustic pressure distribution for different filling ratios, indicating that the pressure peaks at the focal point and decayed with distance, consistent with previous literature. Figure 3e further demonstrated that focal acoustic pressure increased rapidly below a 40% filling ratio and more gradually beyond this threshold, while the focal length remained relatively stable. In contrast, as shown in Fig. 3f, the beamwidth and directivity were largely unaffected by the filling ratio.

Furthermore, a 3D spatial acoustic field of the PMUT array was calculated. As shown in Fig. 3g, the spatial distribution of acoustic pressure remained generally uniform across the same area. However, with increased element density, enhanced crosstalk between PMUT cells led to a progressive transition of the sound pressure distribution from the near field to the far field, as presented in Fig. 3h–i. Although the number of PMUT elements increased from 49 to 169, the overall array aperture remained constant, resulting in an unchanged acoustic emission area and a stable number of near-field interference lobes at a fixed imaging distance. The directivity of the PMUT array was largely insensitive to the filling ratio, which can be attributed to the constant overall aperture size and operating wavelength across all configurations. The primary influence of increasing element density was the intensification of fluid-coupled crosstalk, which complicated phase interactions. This effect manifested as blurred emission profiles and overlapping interference patterns in the X–Y plane rather than altering the number of lobes. Furthermore, experimental observations showed that increasing the filling ratio yielded only a marginal increase in peak pressure (~6 kPa) but a substantial bandwidth broadening (~45%), confirming that crosstalk suppressed the vibration amplitude of individual elements while promoting a far-field-like energy distribution even within the near-field region. This effect was beneficial for improving the spatial resolution of the array in ultrasound imaging applications. Nevertheless, crosstalk also suppressed the individual vibrational amplitude of the cells, resulting in a marked reduction in ultrasonic emission efficiency. Consequently, although the overall output power and acoustic pressure of the array exhibited gradual improvement with increasing crosstalk, the enhancement rate was significantly limited. These results highlighted the critical influence of the filling ratio on the primary acoustic performance metrics of PMUT arrays and provided a design reference for performance optimization. Appropriate adjustment of the filling ratio can minimize inter-cell crosstalk, thereby enabling further enhancement of acoustic output and imaging resolution.

The effect of array size on the performance of PMUT

The effect of array size on the performance of PMUT was evaluated under a fixed spacing of 40 μm and a constant filling ratio of 47.5%. The PMUT array configurations used in the analysis were depicted in Fig. 4a, corresponding to array sizes of $1 \times 1\ \mathrm{mm}^2$, $1.5 \times 1.5\ \mathrm{mm}^2$, $2 \times 2\ \mathrm{mm}^2$, $2.5 \times 2.5\ \mathrm{mm}^2$, and $3 \times 3\ \mathrm{mm}^2$, comprising 36, 81, 144, 196, and 289 elements, respectively. As shown in Fig. 4b, the frequency response with acoustic power across the range of 0–4 MHz revealed that the peak acoustic power was achieved at the array's resonance frequency. Since the inter-element spacing was held constant, the mutual radiation acoustic pressure remained unchanged, resulting in consistent resonance frequencies among arrays of varying sizes. With increasing array size, the maximum acoustic transmitting power per unit voltage exhibited a substantial rise, from 2.1 mW to 17.9 mW, while the transmitting bandwidth remained relatively stable, as illustrated in Fig. 4c. Figure 4d displayed the acoustic pressure in the central axis, where all array sizes showed peak sound pressure at the focal point, decreasing with increasing axial distance from the array surface. As detailed in Fig. 4e, the focal acoustic pressure increased from 109.8 kPa to 132.1 kPa as the array expanded from $1 \times 1\ \mathrm{mm}^2$ to $3 \times 3\ \mathrm{mm}^2$, accompanied by an increase in focal length from 1 mm to 8.2 mm. The effect of array size on acoustic field directivity was further presented in Fig. 4f. A clear narrowing of beamwidth was observed, decreasing from 82° to 36° as the array size increased, while sidelobe levels remained nearly unchanged. These results indicated that increasing the edge length of the array enhanced the acoustic directivity of the PMUT array. Figure 4g presented the spatial acoustic pressure distribution of the PMUT array within a $6 \times 6 \times 12\ \mathrm{mm}^3$ region as the array size enlarged from $1 \times 1\ \mathrm{mm}^2$ to $3 \times 3\ \mathrm{mm}^2$ with a fixed spacing of 40 μm. As the array size expanded, the spatial extent of the acoustic pressure field also increased, with corresponding growth observed in both the focal region and the Rayleigh distance. Due to the fixed array density, the mutual radiation acoustic pressure between PMUT cells remained unchanged with the increasement of elements number. Consequently, the near-field crosstalk and its spatial distribution were largely consistent across configurations. However, the mainlobe length and width of the acoustic pressure field exhibited notable increases, as illustrated in Fig. 4h–i. These results revealed that, with increasing array size, the spatial extent of the acoustic field expanded, while the transmitting bandwidth remained largely

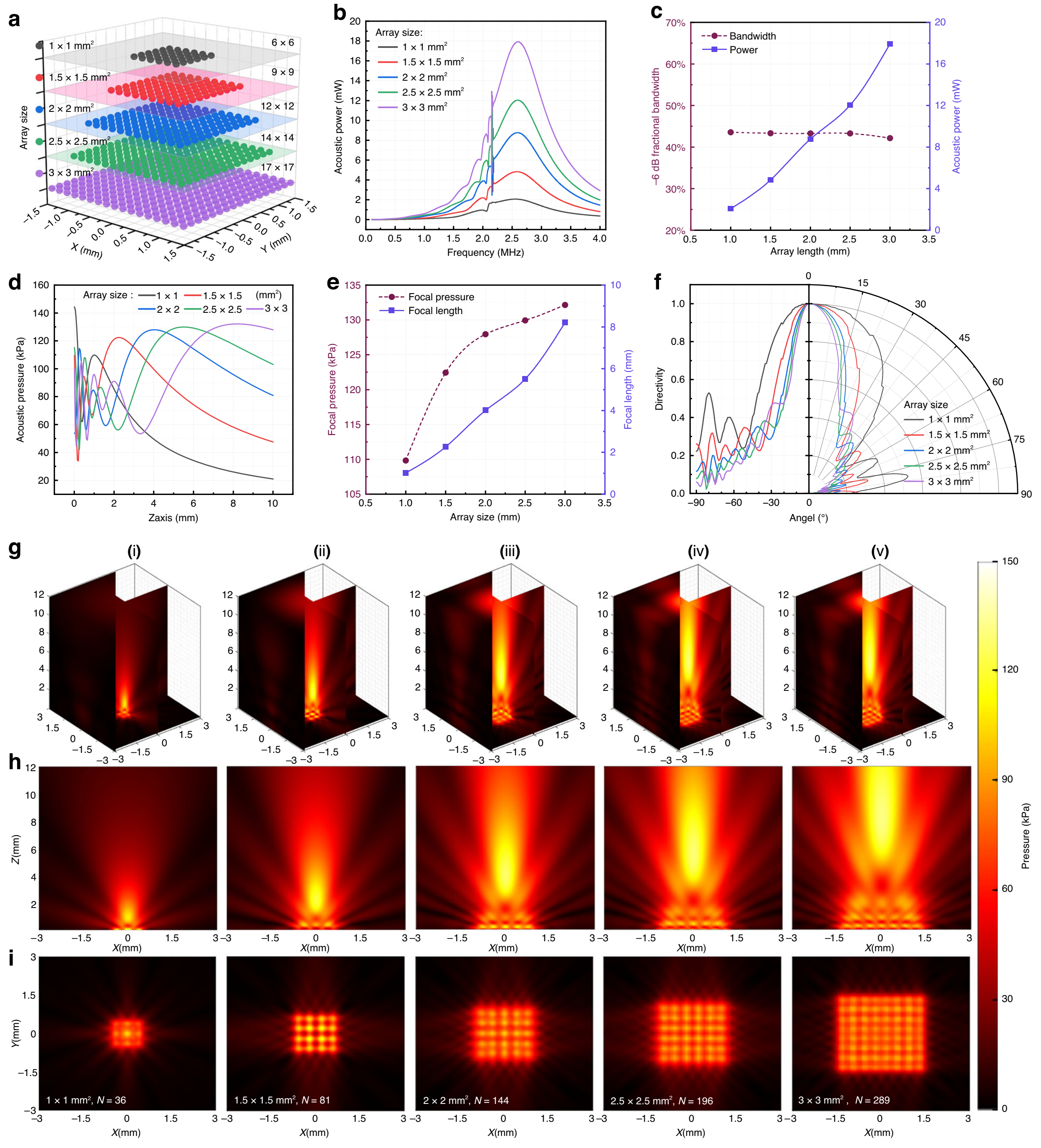

Fig. 4 The effect of array size on the acoustic performance of PMUT arrays. **a** Schematic of PMUT array with the size ranging from 1 × 1 mm^2 to 3 × 3 mm^2. **b** The frequency response of acoustic power. **c** Variations in the -6 dB fractional bandwidth and acoustic output power. **d** Transmitting acoustic pressure along the central axis of the PMUT array. **e** Variations in the focal pressure and length. **f** The directivity of the acoustic beam. **g** Cross-sectional view of the theoretical 3D spatial sound pressure distribution of PMUT arrays in a 6 × 6 × 12 mm^3 area. **h** Acoustic pressure distribution in the central X-Z plane. **i** Acoustic pressure distribution in the X-Y plane (Z = 1 mm)

unchanged. This behavior facilitated enhanced acoustic energy concentration, thereby improving the array's effectiveness in applications such as ultrasonic imaging and high-resolution sensing.

The effect of array arrangement on the performance of PMUT

The influence of different array arrangements on the performance of PMUT arrays was systematically analyzed under fixed element spacing (40 μm) and a constant array size of $2 \times 2\ \mathrm{mm}^2$. Various configurations were analyzed, including square, staggered, hexagonal, octagonal, Fermat, and annular arrays (Fig. 5a-i to a-vii), consisting of 121, 144, 127, 120, 130, and 136 cells, respectively[35]. To ensure a consistent total cell number and occupied area, the annular array was designed with an inner diameter of 1 mm and an outer diameter of 1.5 mm. The frequency response with acoustic power for the different array arrangements were presented in Fig. 5b. Among them, the annular array exhibited the highest acoustic power, whereas the hexagonal array achieved the broadest bandwidth (Fig. 5e). These differences can be attributed to the varying degrees of mutual radiation acoustic pressure: the reduced crosstalk in the annular array enhanced acoustic power output while limiting bandwidth. The theoretical axial acoustic pressure distributions were shown in Fig. 5c. Despite variations in configuration, the focal length for solid PMUT arrays with identical sizes showed minimal change (deviation < 1 mm), confirming that the focal length was primarily determined by the array size. The square array produced the lowest focal pressure, whereas the circular-based configurations (hexagonal, octagonal, Fermat, and annular) demonstrated improved in-phase wave superposition, resulting in higher focal pressures. This discrepancy arose from geometric differences; for example, the square array's corner elements contributed to greater phase mismatches compared to radially symmetric layouts. Additionally, Fig. 5d, g illustrated the effect of array configuration on acoustic beam directivity. Most solid arrays exhibited similar mainlobe widths, while the annular array displayed the narrowest beam (approximately 40% narrower), enhancing axial directivity. However, due to its ring geometry, the annular array radiated acoustic pressure both inward and outward, producing largest sidelobe level compared to other configurations. These findings underscored the critical role of array arrangement in the characteristics of PMUT arrays for targeted applications.

As shown in Fig. 5h, the spatial sound pressure distributions of various array configurations were further examined based on the theoretical PMUT model within a $6 \times 6 \times 10\ \mathrm{mm}^3$ region. Due to its larger occupied area, the square array exhibited a broader spatial mainlobe compared to other solid configurations under identical spacing and array size constraints. For the annular configuration, acoustic pressure was radiated toward the central axis, forming a primary mainlobe, while simultaneous outward radiation produced a surrounding annular sidelobe with elevated sound pressure levels. As depicted in Fig. 5i–j, the acoustic focusing performance of the mainlobe progressively improved from square to circular configurations, accompanied by a reduction in sidelobe levels. As for annular array, sound waves were emitted simultaneously toward both the inner and outer diameters, resulting in a divergent spatial radiation field with multiple distinct sidelobes. These results highlight the effect of array arrangements on the key performance metrics of PMUT array. The studied configurations can be broadly categorized into solid and annular types. As demonstrated in Fig. 5g, i, solid arrays exhibited tightly focused sound pressure within the mainlobe and minimal sidelobe interference, making them more suitable for transmitting applications. In contrast, the annular array produced a distinct central mainlobe accompanied by a prominent ring-shaped sidelobe region, yielding a broader spatial reception area and enhanced sensitivity, thus demonstrating potential advantages for receiving applications.

Result and discussion

Fabrication of PMUT arrays

To validate the performance variation rules derived from the theoretical analysis of array structural parameters, several PMUT array chips were designed and fabricated. Experimental characterizations were performed on the fabricated devices, and the results were compared with the theoretical predictions obtained from the established analytical expressions. As illustrated in Fig. 1a, the PMUT element comprised a piezoelectric actuation layer, an insulating layer, a structural layer, and a substrate layer. The piezoelectric stack included a bottom composite electrode (100 nm Ti/Pt), a buffer layer (20 nm $\mathrm{LaNiO_3}$), a piezoelectric film (1 μm $\mathrm{Pb(Zr_{0.5}Ti_{0.5})O_3}$), and a top electrode (250 nm Au/Cr). The structural silicon layer had a thickness of 5 μm, with a membrane cavity radius of 70 μm. To optimize vibrational displacement, the top electrode coverage was designed at approximately 67% of the membrane area[18]. The element spacing was maintained at 40 μm. The fabrication process of the PMUT based on PZT film had been described in detail in our previous work[15]. The main fabrication steps were summarized in Fig. 6a. First, a 100 nm $\mathrm{SiO_2}$ insulating layer was thermally grown on the top silicon of the SOI wafer (step (i)). A Ti/Pt layer was deposited to form the bottom electrode (step (ii)), followed by sputtering of a 20 nm $\mathrm{LaNiO_3}$ buffer layer (step (iii)). Subsequently, a 1 μm PZT film was deposited, and photolithography was performed to expose the bottom electrode pads (step (iv)). The top electrode was fabricated by first depositing a 20 nm Cr adhesion layer followed by a 250 nm Au layer using magnetron sputtering. The Au/Cr stack was subsequently patterned through a standard photolithography and lift-off process to define the top electrode on the PZT vibrating region (step (v)). Finally, circular cavities were etched on the backside of the substrate via deep reactive ion etching (DRIE) to release the membranes (step (vi)). The fabricated piezoelectric layer exhibited excellent

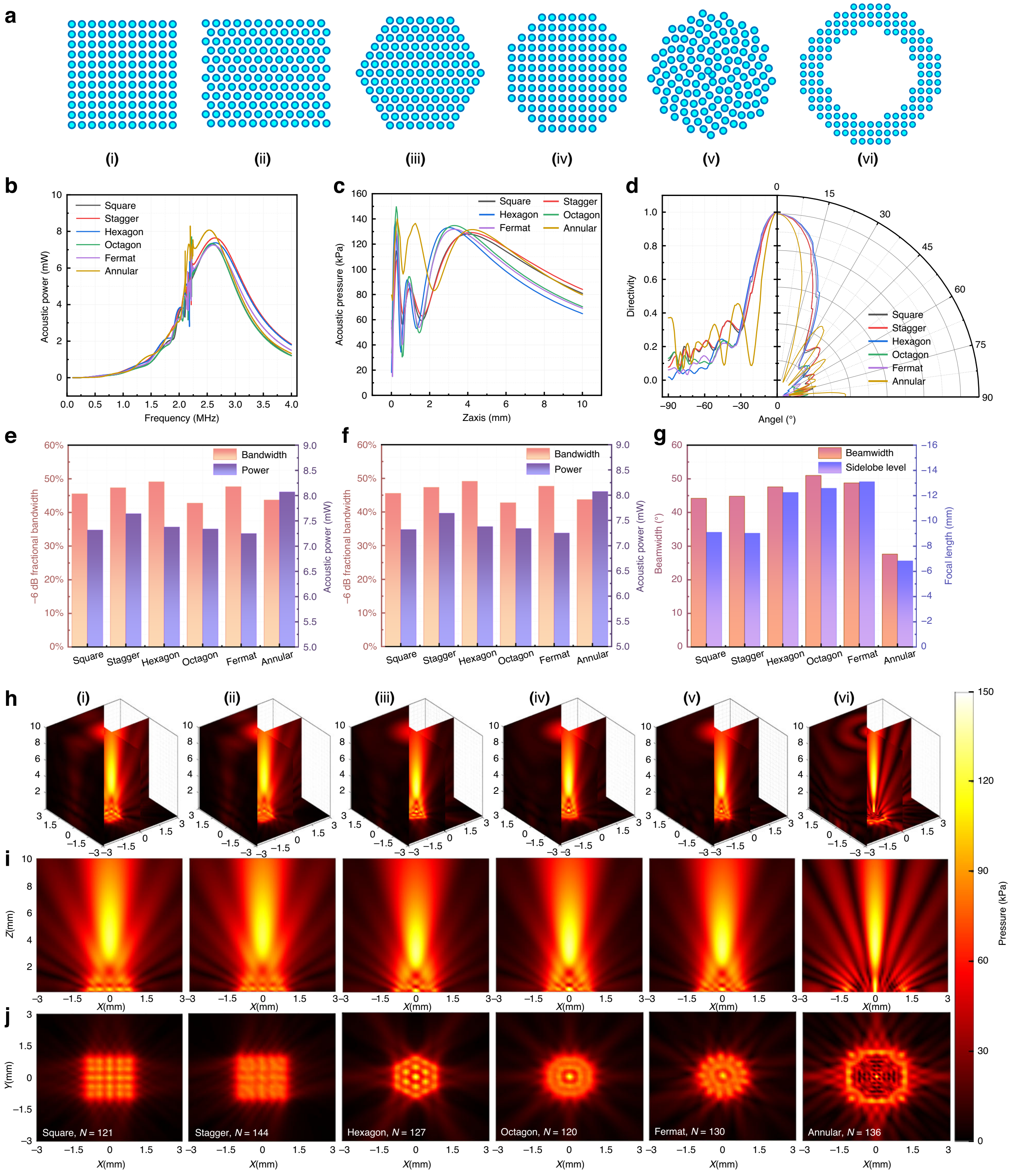

Fig. 5 The effect of array arrangement on the acoustic performance of PMUT arrays. a Schematic of PMUT array with the configuration about square array (121 cells), staggered array (144 cells), hexagonal array (127 cells), octagonal array (120 cells), Fermat array (130 cells) and annular array (136 cells) respectively. **b** The frequency response of acoustic power. **c** Transmitting acoustic pressure along the central axis of the PMUT array. **d** The directivity of the sound field. **e** Variations in the -6 dB fractional bandwidth and acoustic output power. **f** Variations in the focal pressure and length. **g** Variations in the beamwidth and sidelobe level. **h** Cross-sectional view of the theoretical 3D spatial sound pressure distribution of PMUT arrays in a $6 \times 6 \times 12\,\mathrm{mm}^3$ area. **i** Acoustic pressure distribution in the central X-Z plane. **j** Acoustic pressure distribution in the X-Y plane (Z = 1 mm)

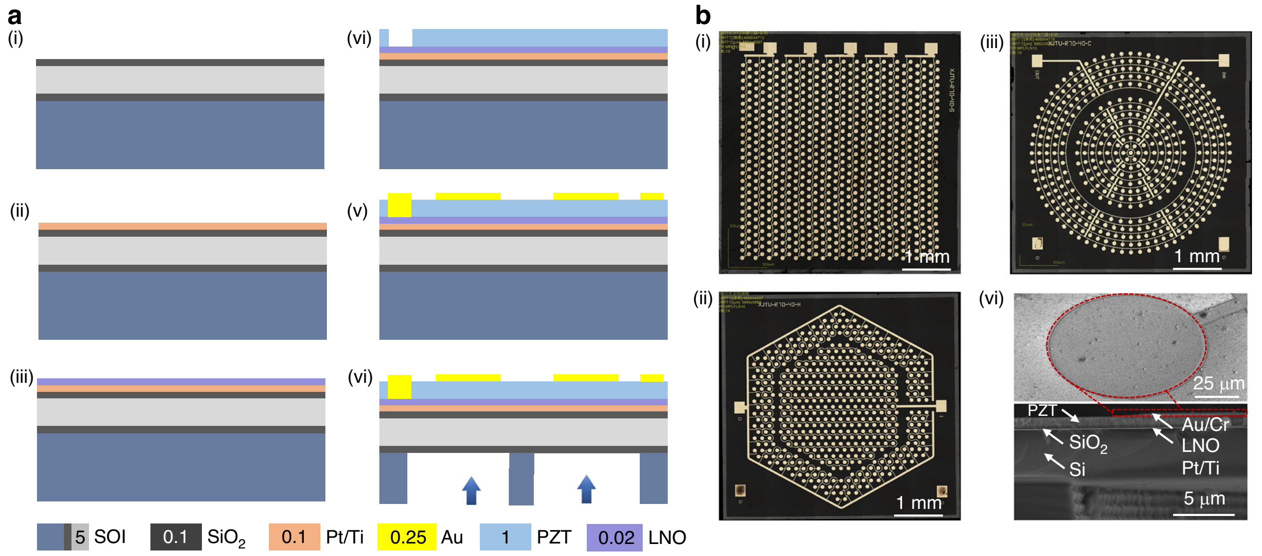

Fig. 6 Characterization of the fabricated PMUT chip. a The fabrication process of PMUT. **b** The optical microscope image of the fabricated PMUT arrays

material properties, including a low processing temperature (480 °C), high piezoelectric coefficient (15.5 C/m²), and low dielectric constant (750). Figure 6b displayed the fabricated PMUT arrays, including: a square array ((i), 784 cells), a hexagonal array ((ii), 547 cells), and a circular-annular array ((iii), comprising 148 and 308 cells), all with an active area of 4.8 × 4.8 mm². A cross-sectional SEM image of a representative PMUT cell was shown in Fig. 6b-(iv), confirming the structural integrity and dimensional consistency of the multilayer.

Characterization for the performance of PMUT arrays

The experimental results characterizing the performance of the fabricated PMUT array chips were presented in Fig. 7. Figure 7b showed the measured electrical impedance of the PMUT arrays obtained using an impedance analyzer (E4990A, Keysight Technologies, USA). The measured resonant frequencies in air were 2.848 MHz for the square array, 2.798 MHz for the hexagonal array, 2.815 MHz for the circular array, and 2.818 MHz for the annular array. These variations in resonant frequency, despite identical cavity sizes, were attributed to differences in cell number and array arrangement, which modulated the mutual radiation acoustic pressure effects among the elements. Each array comprised several hundred PMUT cells connected in parallel, resulting in a combined electrical impedance of less than 10 Ω. This low impedance reflected minimal signal mismatch loss and indicated favorable conditions for efficient impedance matching with backend drive and receiving circuits.

Furthermore, the acoustic performances of the PMUT arrays were evaluated[36] using a calibrated needle hydrophone (NH2000, Precision Acoustics, UK), which was immersed in a silicone oil bath with a kinematic viscosity of 50 cSt. The PMUT chips were driven by a function generator (DG-1032Z, Rigol, China), providing a 20 Vpp AC excitation signal with 5 cycles. The acoustic signals were captured by the hydrophone and subsequently processed through a −20 dB attenuator, an 8 dB preamplifier, and a 25 dB RF amplifier (standard for the NH 2000 system). To investigate the influence of array structural parameters on acoustic performance, various PMUT array configurations were considered, including a 784-cell square array, a 547-cell hexagonal array, a 148-cell inner circular array, and a 308-cell outer circular array. As shown in Fig. 2e, the deviation in maximum vibration displacement between the simplified thin-film model and the complete multilayer model was approximately 4.7%, corresponding to a neutral-plane shift of about 300 nm in the complete film. Accordingly, a compensation coefficient $K = 300$ nm was introduced. In addition, the experimentally fabricated PMUT devices exhibited piezoelectric coefficients lower than those of PZT-5H in the FEM material library. Based on the calculated correlations between acoustic performance and deviations in the piezoelectric coefficient and piezoelectric layer thickness (Fig. 2n, p), the effective piezoelectric coefficient used in subsequent calculations was optimized to 210 pC/N. Using this parameter-optimized theoretical model, the acoustic performance of PMUT arrays with different element numbers and array configurations under practical fabrication conditions was further evaluated. This approach ensured both predictive accuracy and practical relevance for fabricated devices. The results were

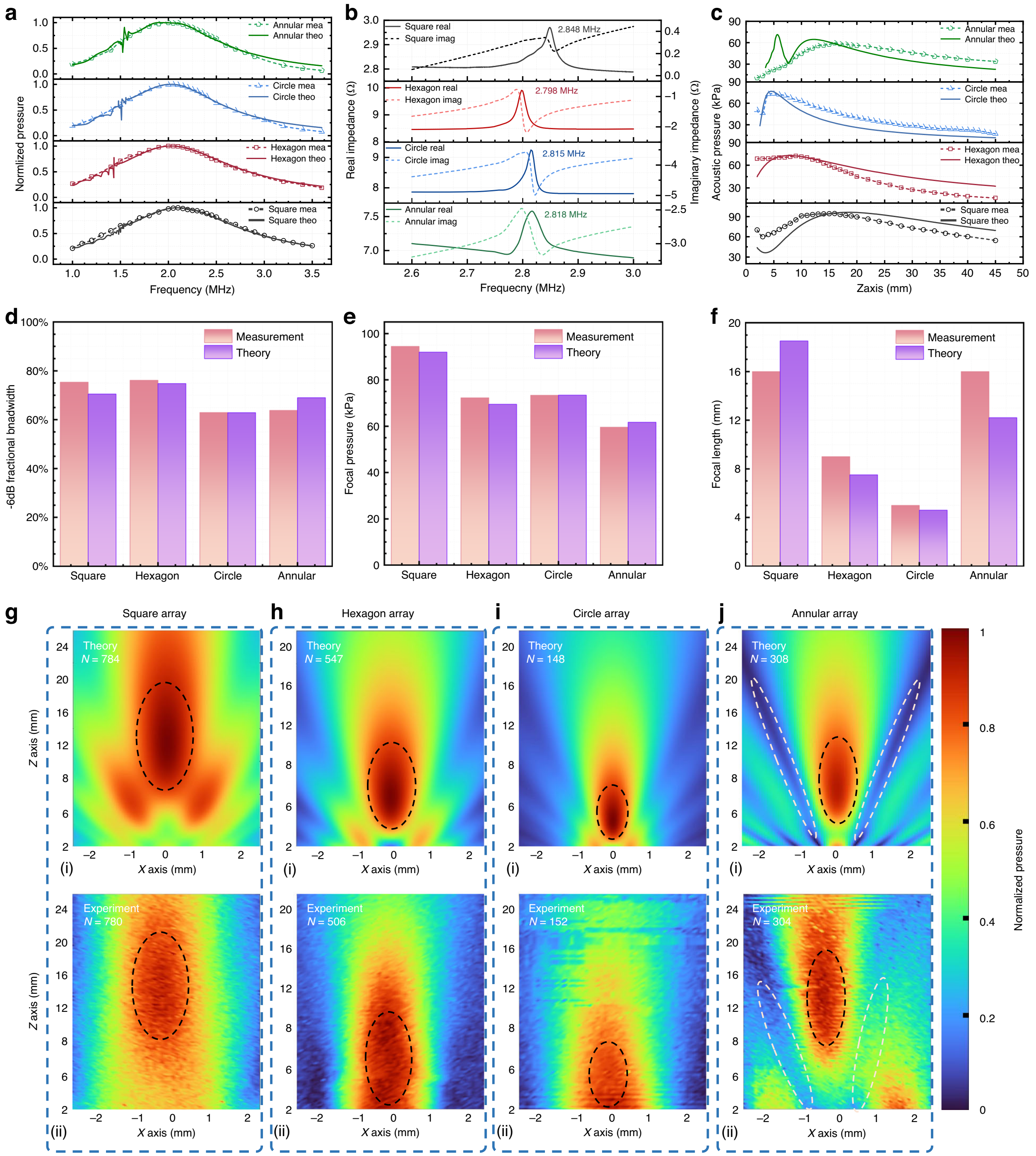

Fig. 7 The experimental measured (Mea) and theoretical calculation (Theo) results for the performance of the PMUT chips. a The measured electrical impedance of the four PMUT arrays. **b** The frequency response with the normalized acoustic pressure. **c** The acoustic pressure along the central axis. **d** Comparative analysis of theoretical and experimental -6 dB fractional bandwidth; **e** Comparative analysis of theoretical and experimental focal pressure; **f** Comparative analysis of theoretical and experimental focal length. **g** Acoustic field of the square array. **h** Acoustic field of the hexagon array. **i** Acoustic field of the inner circle array. **j** Acoustic field of the outer annular array

then compared with experimental measurements to validate the model. As shown in Fig. 7a–f, the experimental acoustic performance of the fabricated PMUT chips was in good agreement with the theoretical predictions. In particular, Fig. 7a presented the frequency response in terms of normalized acoustic pressure, where the

Table 3 The comparison of theoretical and experimental results for the fabricated PMUT arrays

Array arrangement	Parameter	Theory	Measurement	Error
Square array 784-Theo 780-Mea	Frequency (MHz)	2.09	2.10	0.5%
	−6 dB Bandwidth	70.5%	75.3%	6.4%
	Output Pressure (kPa)	96.3	94.4	2%
Hexagon array 547-Theo 506-Mea	Frequency (MHz)	2.00	2.03	1.5%
	−6 dB Bandwidth	74.8%	76.1%	1.7%
	Output Pressure (kPa)	72.8	72.2	0.8%
Circle array 148-Theo 152-Mea	Frequency (MHz)	2.05	2.02	1.5%
	−6 dB Bandwidth	62.9%	63%	0.8%
	Output Pressure (kPa)	76.9	73.3	4.8%
Annular array 308-Theo 304-Mea	Frequency (MHz)	2.00	1.91	4.7%
	−6 dB Bandwidth	69%	63.8%	8.1%
	Output Pressure (kPa)	64.6	59.6	8.4%

experimental frequency curves closely followed the trends predicted by the theoretical model for all array configurations around 2 MHz, demonstrating the reliability of the developed analytical expressions. As shown in Fig. 7d, despite the variations in the array arrangement, the experimental −6 dB bandwidth closely matched approximately 70% of the theoretical calculation results. In Fig. 7c, a comparison of the acoustic pressures for various array arrangements was presented. Both theoretical and experimental results demonstrated comparable variation trends as the axial distance increases. Figure 7e presented a comparison between the theoretical and experimental focal acoustic pressures for the different array arrangements. Despite identical sizes and spacings for each PMUT chips, variations in cells number within the same footprint area led to differences between experimental measurements and theoretical predictions, as discussed in the section of array arrangement. The analysis validated that the output acoustic pressure increased with the number of cells, a trend that was consistently supported by both experimental data and theoretical results. Furthermore, the investigation of various array configurations revealed distinct influences on acoustic focusing capability and output performance. A comprehensive comparison between the experimentally measured and theoretically calculated results for the fabricated PMUT arrays was provided in Table 3, offering a quantitative assessment of model accuracy and performance trends. As shown in Fig. 7c–f, the circular boundary design effectively mitigated inter-element crosstalk, leading to a more concentrated acoustic field and enhanced pressure output. Remarkably, despite its significantly reduced number of elements (152 cells in the circular array versus 784 cells in the square array), the circular array achieved an output pressure (73.3 kPa experimentally, 76.9 kPa theoretically) that was comparable to that of the square array (94.4 kPa experimentally, 96.3 kPa theoretically), with only limited degradation. A similar trend was observed in the hexagonal array (506 cells), which exhibited consistent performance with output pressures of 72.2 kPa experimentally and 72.8 kPa theoretically. In contrast, the annular array, with its lower element density and more dispersed radiation region, demonstrated weaker acoustic focusing, particularly at short focal distances. Both experimental (59.1 kPa) and theoretical (64.6 kPa) results confirmed that this configuration yielded the lowest focal acoustic pressure, though it simultaneously produced a relatively larger focal length. Figure 7f compared the focal lengths derived from experimental measurements and theoretical predictions across the different array configurations. The results showed close alignment between theory and experiment, with focal lengths of 16 mm/18.5 mm for the square array, 9 mm/7.5 mm for the hexagonal array, 5 mm/4.6 mm for the circular array, and 16 mm/12.2 mm for the annular array. These consistent trends further highlight that the spatial distribution and focusing behavior of the acoustic field are highly sensitive to array geometry, underscoring the importance of configuration optimization in PMUT array design.

A comprehensive analysis of the acoustic pressure distribution revealed that the discrepancy between the measured sound pressure values and the theoretical predictions was primarily attributed to variations in the resonant frequencies among individual elements within the fabricated PMUT array, as well as potential phase inconsistencies during actuation. Furthermore, deviations in membrane thickness resulting from manufacturing processes, material inhomogeneity, and the complexity of boundary conditions may also contribute to the observed non-uniformity in the acoustic performance of the array. The acoustic field distribution areas for different array configurations were further analysed. Due to discrepancies between the experimental and theoretical results, the color intensity of the acoustic field maps for each array at the same sound pressure level varied, complicating direct comparisons of their acoustic focusing regions. To mitigate this issue, the sound pressure values in the spatial acoustic field were normalized, which allowed for clearer identification of the focal areas and facilitated accurate comparisons of the acoustic field distributions across the different array configurations. Figure 7g–j depicted the theoretically calculated and experimental measured acoustic field distributions for PMUT arrays with different structural configurations. The focal acoustic areas, indicated by black dotted lines, showed strong agreement between experimental measurements and theoretical calculations for the square, hexagonal, circular, and annular arrays. This consistency suggested that the experimental sound pressure distribution and focal positions closely matched the theoretical predictions. These results collectively validated the accuracy and reliability of the proposed theoretical framework for characterizing array performance, particularly in establishing a clear relationship between geometric design parameters and spatial field focusing capabilities.

To further evaluate the practical performance of the fabricated PMUT arrays, a pulse-echo measurement system was established, as illustrated in Fig. 8a. A 2 mm-thick reflector was mounted on a high-precision XYZ displacement stage and positioned 40 mm away from the center of the PMUT arrays. A pulser-receiver (CTS-8077PR, SIUI, China) was employed to generate the excitation signal for ultrasound transmission and to simultaneously capture the echo signals reflected from the target, which were then recorded using an oscilloscope. As depicted in Fig. 8b, the reflector was laterally shifted along the X-axis in 1 mm steps over a range of 0–10 mm to characterize the spatial response of the arrays. Figure 8c–g indicated that all array configurations exhibited excellent transmit-receive sensitivity within the 0–5 mm lateral displacement range. Specifically, the square array showed the most rapid acoustic attenuation, the hexagonal array demonstrated a more uniform response distribution, and the circular array maintained the most consistent acoustic decrease. In contrast, the annular array, due to its larger side lobes, distributed acoustic field energy not only in the main lobe but also in other directions. leading to a stronger initial echo followed by partially overlapping secondary echoes. Benefiting from its far-field focusing characteristics, the annular array continued to receive detectable echoes even at displacement of 8–10 mm, exhibiting a relatively stable acoustic attenuation trend. These results systematically validated the directional characteristics and practical performance of each array under realistic operating conditions.

Prospects for the application of PMUT array design

The aforementioned results highlight the effect of key structural parameters on the performance of PMUT arrays, such as filling ratio, array size, array and arrangement. In summary, high filling ratio enhances transmission power, bandwidth, and focal-plane acoustic pressure. Transmission power, focal length, and beamwidth are directly proportional to the array size. Circular and Fermat spiral arrays offer better focal-plane acoustic pressure and lower sidelobe levels compared to square arrays. While the annular array provides a broader acoustic radiation area, it also exhibits increased sidelobes, reduced bandwidth, and a narrower beamwidth relative to conventional array configurations.

The design of PMUT arrays can be tailored to the specific requirements of the practical application, with careful consideration of performance parameters such as focal length, beamwidth, and sidelobe levels. In ultrasonic imaging applications[37], a higher filling ratio increases bandwidth and enhances image resolution, while larger array size improves both transmitting and receiving performance, extends near-field detection, and narrows the beamwidth. Configurations like Fermat spiral and circular-like arrays (e.g., hexagonal, octagonal) offer improved focused acoustic pressure and reduced sidelobes, which enhance resolution. For ultrasonic therapy applications[35,38], the circular array provides high focal sound pressure and narrow beamwidth, ideal for precise pressure concentration, with larger array further boosting output power. In ultrasonic time-of-flight (TOF) applications, such as distance detection and flow measurement[39], circular-like arrays are beneficial for short-range detection due to their smaller near-field distance[40], larger beamwidth, and higher output pressure. For long-range detection, larger array increases far-field sound pressure, and Fermat spiral array further enhances far-field performance while minimizing acoustic crosstalk. Annular array, with their narrow main lobe and large sidelobes, offers high sensitivity to acoustic fluctuations, making them suitable for wide-area reception applications. Both theoretical and experimental results demonstrate that the filling factor is positively correlated with sound pressure and bandwidth, while the array size predominantly influences the detection range and beam characteristics. The array configuration plays a key role in determining focusing efficiency and sidelobe levels. Therefore, optimizing array parameters is essential to strike a balance between detection accuracy and overall performance.

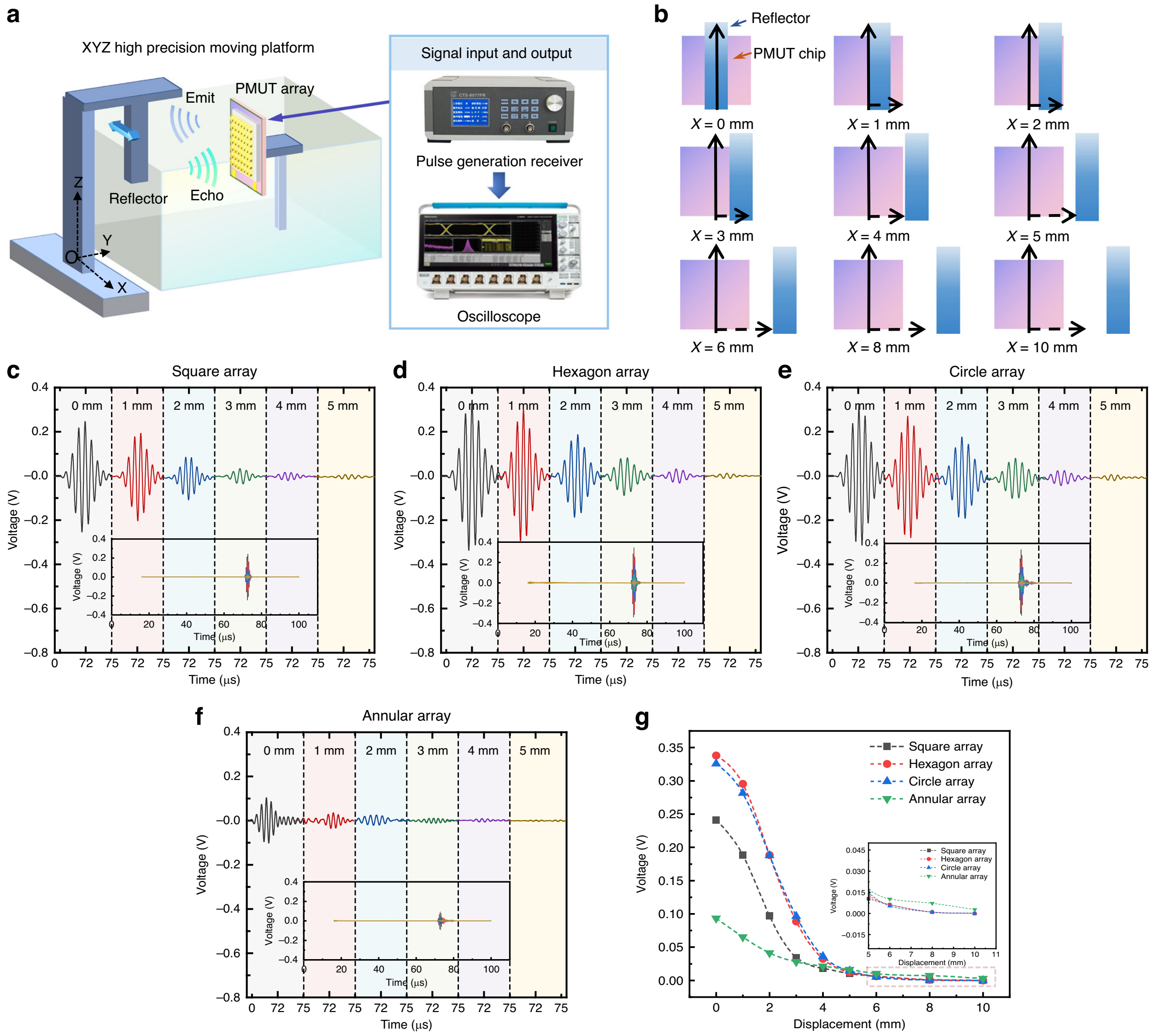

Fig. 8 The pulse-echo spatial response characterization of PMUT arrays. a Schematic of the pulse-echo measurement system. **b** Lateral movement of the reflector along the X-axis in 1 mm steps within a range of 0–10 mm for spatial response characterization. **c** Echo response as a function of reflector displacement for the square array. **d** Echo response as a function of reflector displacement for the hexagonal array. **e** Echo response as a function of reflector displacement for the circular array. **f** Echo response as a function of reflector displacement for the annular array. **g** Comparison of echo attenuation trends across all PMUT arrays

Moreover, to validate the practical applicability of the our theories for large-scale applications, a detailed computational study on large PMUT arrays, including performance predictions for 20 × 20 to 100 × 100 PMUT arrays, was provided in the Supplementary Materials (Table S1, Fig. S15 and S16). The total acoustic power increased proportionally with the number of elements, with peak sound power rising from 43 mW for a 20 × 20 array to 273 mW for a 100 × 100 PMUT array. This result was consistent with the aforementioned discussed trend of array performance as a function of size. For the 100 × 100 PMUT array, the theoretical results indicated a focal distance of 330 mm and a focal sound pressure of 133 kPa. The sound pressure was primarily distributed in the far-field, with a focusing range extending from 150 mm to 600 mm, and a focal area of approximately 10 mm × 450 mm. However, high-precision computation for the 7 × 7 PMUT array using the finite element method consumed approximately 85 h on the workstation, whereas the theoretical model required a mere 0.06 min. When the array size increased to 100 × 100, FEM simulations became impractical due to exponentially growing computational costs, with simulation time and resource consumption increasing drastically. In contrast, the theoretical model maintained high accuracy while significantly reducing the computational burden, requiring only 175.39 min to calculate the 100 × 100 PMUT array. These results highlighted the computational advantage of the theoretical model for large-scale array optimization, making it highly suitable for real-world applications.

Conclusion

This study proposed a novel electro-mechanical-acoustic coupling model for PMUT arrays, incorporating an analytical expression of the vibration distribution function for individual element and the mutual radiation acoustic impedance between elements. This approach overcame the limitations of existing theoretical models in accurately analysing large-scale arrays and enabled comprehensive prediction of key acoustic performance metrics, including transmission power, bandwidth, focal pressure, and directivity. The model's accuracy was validated by FEM simulations, with a deviation of less than 3%. Parametric analysis showed that increasing the filling ratio from 20% to 60% enhanced transmission power (6.65 mW to 8.15 mW) and bandwidth (16.4% to 59%), but also intensified crosstalk, thereby reducing acoustic focusing efficiency. Similarly, enlarging the array size from $1 \times 1\ \text{mm}^2$ to $3 \times 3\ \text{mm}^2$ significantly boosted transmission power (2.1 mW to 17.9 mW) and focal pressure (109.8 kPa to 132.1 kPa), while narrowing the beamwidth from 82° to 36°, enhancing directivity. The array configuration also impacted performance: square array showed high crosstalk with low focal pressure, circular-like arrays provided better focal pressure with a shorter focal length, and annular array with its mainlobe and ring-shaped sidelobes, was well-suited for long-range focusing and delivering higher focal pressures at greater distances. The experimental results of fabricated PMUT arrays (square, hexagonal, circular, and annular) were in good agreement with the theoretical predictions, validating the proposed ECM.

This work presents a generalized equivalent circuit model for PMUT arrays. A key innovation is the development of a simplified, yet highly accurate, two-layer membrane model that incorporates a correction factor to improve computational efficiency while maintaining precision. This framework enables the first analytical calculation of critical performance metrics- such as power, bandwidth, and acoustic field- for PMUT arrays with arbitrary element arrangements and filling ratios, addressing limitations in prior models restricted to single-element or fixed configurations. This work provides valuable insights into PMUT array optimizing in biomedical imaging, non-destructive testing, and underwater sensing. Experimental validation and detailed parameter analysis offer a reliable framework for designing PMUT arrays with enhanced performance in transmission power, bandwidth, and acoustic focusing. In the future, we will focus on integrating optimization algorithms and intelligent control strategies to balance performance, power consumption, and cost, thereby advancing PMUT array deployment in emerging fields such as wearable electronics, neural modulation, and microrobotics.

Acknowledgements
This work was supported in part by the National key Research and Development Program of China under Grant 2023YFF0720800, in part by the National Natural Science Foundation of China under Grant 52435010 and 52275570, and in part by the Chinese Institutes for Medical Research under Grant CX23YZ08.

Author details
[1]State Key Laboratory for Manufacturing System Engineering, State Industry-Education Integration Center for Medical Innovations, International Joint Laboratory for Micro/Nano Manufacturing and Measurement Technologies, Shaanxi Innovation Center for Special Sensing and Testing Technology in Extreme Environments, Shaanxi Provincial University Engineering Research Center for Micro/Nano Acoustic Devices and Intelligent Systems, Xi'an Jiaotong University, Xi'an, China. [2]School of Mechanical Engineering, Xi'an Jiaotong University, Xi'an, China. [3]Shandong Laboratory of Yantai Advanced Materials and Green Manufacturing, Yantai, China. [4]School of Instrument Science and Technology, Xi'an Jiaotong University, Xi'an, China. [5]Cardiac Surgery, Beijing Anzhen Hospital, Capital Medical University, Beijing, China. [6]National Local Joint Engineering Research Center for Precision Surgery and Regenerative Medicine, Shaanxi Provincial Center for Regenerative Medicine and Surgical Engineering, Department of Cardiology, the First Affiliated Hospital of Xi'an Jiaotong University, Xi'an, China

Author contributions
Zixuan Li conceived the experiment, studied the detection principle, performed the simulations, fabricated the device, and drafted the manuscript and figures. Jiawei Yuan, Yihe Zhao and Shaohui Qin assisted in the fabrication process of PMUT. Hongqiang Tan, Zilong Zhao and Zimeng Zhang assisted in the experiment. Dejiang Lu contributed to the revision and proofreading of the manuscript. Zhikang Li, Xiaozhang Wang, Min Li, Lihong Fan and Libo Zhao initiated the project, provided input to the manuscript, and provided the resources and supervision.

Conflict of interest
The authors declare no competing interests.

Supplementary information The online version contains supplementary material available at https://doi.org/10.1038/s41378-026-01159-7.

Appendix

Appendix A

The expressions for M_p and σ_p are given by:

$$M_p = \sigma_p h_p Z_p \tag{A1}$$

$$\sigma_p = e_{31,f} E_p \tag{A2}$$

Where $e_{31,f}$ is the modified transverse piezoelectric coefficient, and V_{in} is the input alternating voltage between upper and lower electrodes, with $V_{in}=E_p h_p$.

By substituting the general solution Eq. (7) into the vibration control equation (Eq. (4)), the homogeneous control equation can be given as:

$$\nabla^4 W - \beta^4 W = 0 \tag{A3}$$

$$\beta^4 = \frac{\rho_s \omega^2}{D} \tag{A4}$$

The generalized solution[41] of above Eq. (A3) is expressed as follow:

$$W(r,\theta) = [C_1 J_n(\beta r) + C_2 Y_n(\beta r) + C_3 I_n(\beta r) + C_4 K_n(\beta r)]\cos(n\theta) \tag{A5}$$

Where, C_1, C_2, C_3, C_4 are undetermined coefficients; J_n- Bessel function of the first kind; I_n- modified Bessel function of the first kind; Y_n- Bessel function of the second kind; K_n- modified Bessel function of the second kind; n- vibration mode order.

When the circular membrane is in a low-order resonance state, its axisymmetric vibration mode dominates. Therefore, this paper only discusses the axisymmetric vibration mode represented by $n = 0$. Given that the displacement at the center of the circular membrane ($r = 0$) is finite, and the second and fourth terms in Eq. (A5) do not converge at $r = 0$. The boundary conditions of the circular membrane can only impose constraints on the deflection and radial slope at the clamped edge. Consequently, the coefficients C_2 and C_4 are set to zero, while C_1 and C_3 are determined by solving the clamped boundary conditions at the periphery of the membrane:

$$\begin{cases} C_1 J_n(\beta a) + C_3 I_n(\beta a) = 0 \\ \frac{\partial}{\partial r}[C_1 J_n(\beta r) + C_3 I_n(\beta r)]\big|_{r=a} = 0 \end{cases} \tag{A6}$$

To ensure the existence of a nonzero solution to the above equation, its coefficient matrix must be 0, which leads to:

$$J_n(\beta a) I_{n+1}(\beta a) + J_{n+1}(\beta a) I_n(\beta a) = 0 \tag{A7}$$

$$\beta_i^2 = \frac{\beta^2 r_c^2}{\pi^2} = \sqrt{\frac{\rho_s}{D}}\frac{r_c^2}{\pi^2}\omega_i \tag{A8}$$

For a specific loading condition at the radial x, the particular solution of Eq. (A3) can be expressed by the Green's function $G(r\,|\,x)$[28]. The control equation under the unit loading condition can be given as:

$$\left(\nabla^4 - \beta^4\right) G(r|x) = \frac{\delta(r-x)}{r} \tag{A9}$$

The particular solution of this differential equation can also be expressed as a linear superposition of a series of general solutions. Therefore, $G(r\,|\,x)$ can be represented as:

$$G(r|x) = \sum_i A_i \psi_i(r) \tag{A10}$$

$$\psi_i(r) = J_0\left(\frac{\pi\beta_i}{r_c} r\right) - \frac{J_0(\pi\beta_i)}{I_0(\pi\beta_i)} I_0\left(\frac{\pi\beta_i}{r_c} r\right) \tag{A11}$$

By substituting Eq. (A10) back into Eq. (A9), and then multiplying by $\psi_j(r)dr$ and integrating over the entire circular surface, we can obtain:

$$\begin{aligned} 2\pi\int_0^{r_c}\psi_j(r)\left[\sum_i A_i\left(\nabla^4 - \beta^4\right)\psi_i(r)\right] rdr \\ = 2\pi\int_0^{r_c}\delta(r-x)\psi_j(r)dr \end{aligned} \tag{A12}$$

Based on the orthogonality of the eigenfunctions, $\psi_j(r)\cdot\psi_j(r) \neq 0$ only when $i \neq j$.Therefore, the coefficient A_i can be determined. Consequently, the Green's function can be expressed as:

$$G(r|x) = \sum_i \frac{\psi_j(r)\cdot\psi_i(x)}{\Lambda_i\left[\left(\frac{\pi\beta_i}{r_c}\right)^4 - \beta^4\right]} \tag{A13}$$

$$\Lambda_i = \int_0^{r_c}[\psi_i(r)]^2 rdr \tag{A14}$$

The vibration equation can be solved by utilizing the properties of Green's function[29]. First, multiply Eq. (4) by $rG(r\,|\,x)$ and Eq. (A9) by $rW(r)$. Subtract the modified equations and perform an integration over the entire plate area. In axisymmetric plate vibration mode, the maximum deflection occurs at the plate center, assumed that $|\partial W/\partial r|_{r=0} = 0$. Given the assumptions of zero slope at the center and clamped boundary conditions, the deflection of the plate derived via integration by parts can be described as:

$$W(x) = \int_0^{r_c} rf(r)G(r|x)dr \tag{A15}$$

Appendix B

The expressions of C_0, Z_{mec}, Z_{aco}, and η can be presented as:

$$C_0 = \frac{\varepsilon\pi r_e^2}{h_p} \tag{B1}$$

$$Z_{mec} = \frac{1}{j\omega Y_m} \tag{B2}$$

$$Z_{\text{aco}} = \frac{Z_{\text{self}}}{\pi r_{eff}^2} \tag{B3}$$

$$\eta = \frac{b_t}{Y_m} \tag{B4}$$

Where ε is the dielectric constant of piezoelectric material, and Z_{self} denotes the self-radiation impedance of an equivalent circular vibration piston. The effective radius r_{eff} of the equivalent circular diaphragm ensures that the model shows the same volumetric displacement as the real vibration condition and can be approximated as $r_{\text{eff}} \approx r_c/\sqrt{3}$.

The PMUT cell is modeled as a flexural diaphragm operating in the d_{31} vibration mode. The transverse vibration velocity distribution $v(r)$ of the clamped circular membrane[42] can be expressed as:

$$v(r) = U \cdot e^{i\omega t}\left[\alpha_0 + \sum_{n=1}^{\infty} \alpha_n \left(\frac{r}{r_c}\right)^n\right], r < r_c \tag{B5}$$

where U is the velocity amplitude. α_n corresponds to the dimensionless coefficients determined by the boundary conditions. For the clamped edge, the boundary conditions ($v = 0$ and $\partial v/\partial r = 0$ at $r = r_c$) lead to the specific values for the first few coefficients that provide sufficient accuracy [3]: $\alpha_0 = 1$, $\alpha_1 = 0$, $\alpha_2 = -2$, $\alpha_3 = 0$, $\alpha_4 = 1$. Thus, the velocity profile $v^*(r)$ is symmetric and dominated by even-powered terms:

$$v^*(r) = U \cdot e^{i\omega t} \sum_{n=1}^{\infty} \alpha_{2n} \left(\frac{r}{r_c}\right)^{2n}, r < r_c \tag{B6}$$

The velocity potential $\psi(r)$ radiated by the vibrating membrane is given by the Rayleigh integral, which is the solution to the Helmholtz equation for a planar source in an infinite baffle[42]:

$$\psi(r) = -\frac{1}{2\pi} \int_0^{2\pi} \int_0^{r_c} v(r) \frac{e^{-ikR}}{R} ds \tag{B7}$$

where k is the wavenumber. R is the distance from a source point on the membrane to the observation point.

$$\psi(r) = -\frac{Ue^{i\omega t}}{2\pi} \sum_{n=0}^{\infty} \alpha_{2n} \int_0^{2\pi} \int_0^{r_c} \left(\frac{r}{r_c}\right)^{2n} \frac{e^{-ikR}}{R} r dr d\varphi \tag{B8}$$

The acoustic pressure at the membrane surface $P(r)$ is the superposition of radiation contributions from all point elements across the entire piston surface. The $P(r)$ can be calculated using the Rayleigh Integral:

$$P(r) = -i\omega\rho\psi(r) = -i\omega\rho c U e^{j\omega t} \sum_{i=0}^{\infty} \alpha_{2i} Z_{2i}(r) \tag{B9}$$

where the functions $Z_{2i}(r)$ is defined by:

$$Z_{2i}(r) = \frac{ik}{2\pi} \int_0^{2\pi} \int_0^{R'} \left(\frac{r'}{r_c}\right)^{2i} e^{-ikR} dR d\alpha \tag{B10}$$

where R' and r' can be expressed as:

$$R' = r\cos\alpha + \sqrt{r_c^2 - r^2 \sin^2\alpha} \tag{B11}$$

$$r' = \sqrt{R^2 + r^2 - 2rR\cos\alpha} \tag{B12}$$

The self-radiation impedance Z_{self} is defined as the ratio of the total force on the membrane to the average volume velocity[43]. It can be calculated by integrating the product of the surface pressure and the conjugate of the complex velocity distribution:

$$Z_{self} = \frac{\iint_S P(r) v^*(r) ds}{\iint_S |v(r)|^2 ds} \tag{B13}$$

Substituting Eq. (B6) and Eq. (B9) into Eq. (B13), the self-radiation impedance becomes:

$$Z_{self} = \frac{2\pi\rho c U^2}{\langle |v| \rangle^2} \sum_i \sum_j \alpha_{2i} \alpha_{2j} \int_0^{r_c} Z_{2i}(r) \left(\frac{r}{r_c}\right)^{2j} r dr \tag{B14}$$

where $\langle |v| \rangle$ is the spatial average of the velocity. For an axisymmetric velocity distribution, the integral can be simplified as:

$$\langle |v| \rangle = \frac{1}{\pi r_c^2} \iint_S |v| ds = 2U \sum_{i=0} \frac{\alpha_{2i}}{2i+2} \tag{B15}$$

Subsequently, the self-radiation impedance Z_{self} of the circular membrane with a radius of r_c can be expressed as:

$$Z_{\text{self}} = \frac{\rho c \pi {r_c}^2}{2\left(\sum_{i=0} \frac{\alpha_{2i}}{2i+2}\right)^2} \sum_{\kappa=0} \sum_{l=0} \left(\alpha_{2\kappa} \alpha_{2l} S_{2\kappa 2l} + j \cdot \alpha_{2\kappa} \alpha_{2l} T_{2\kappa 2l}\right) \tag{B16}$$

$$S_{\kappa \mathrm{l}} = \int_0^1 \mathrm{Re}\left[\mathrm{Z}_{\kappa}\left(\frac{\mathrm{r}}{\mathrm{r_c}}\right)\right] \left(\frac{\mathrm{r}}{\mathrm{r_c}}\right)^{\mathrm{l}+1} \mathrm{d}\left(\frac{\mathrm{r}}{\mathrm{r_c}}\right) \tag{B17}$$

$$T_{\kappa l} = \int_0^1 \mathrm{Im}\left[Z_\kappa\left(\frac{r}{r_c}\right)\right]\left(\frac{r}{r_c}\right)^{l+1} d\left(\frac{r}{r_c}\right) \tag{B18}$$

When $\alpha_0 = 1$ and all other coefficients are 0, the vibration of the entire circular region is equivalent to that of a vibrating piston with an effective radius of r_{eff}. In this case, the self-radiating impedance can be further simplified.

Received: 29 June 2025 Revised: 27 November 2025 Accepted: 12 December 2025

References

1. Qu, M. et al. Sensing and controlling strategy for upper extremity prosthetics based on piezoelectric micromachined ultrasound transducer. *IEEE Trans. Biomed. Eng.* **71**, 1161–1169 (2023).
2. Jiang, X. et al. Ultrasonic fingerprint sensor with transmit beamforming based on a PMUT array bonded to CMOS circuitry. *IEEE Trans. Ultrason. Ferroelectr. Freq. Control* **64**, 1401–1408 (2017).
3. Jung, J. et al. Review of piezoelectric micromachined ultrasonic transducers and their applications. *J. Micromech. Microeng.* **27**, 113001 (2017).
4. Zamora, I., Ledesma, E., Uranga, A. & Barniol, N. Phased array based on AlScN Piezoelectric Micromachined Ultrasound Transducers monolithically integrated on CMOS. *IEEE Electron Device Lett.* **43**, 1113–1116 (2022).
5. Wong, S. J., Roy, K., Lee, C. & Zhu, Y. Thin-film piezoelectric micromachined ultrasound transducers in biomedical applications: a review. *IEEE Trans. Ultrason. Ferroelectr. Freq. Control* **71**, 622–637 (2024).
6. Li, Z. et al. Noninvasive stress detection based on piezoelectric micromachined ultrasonic transducers for bolt loosening warning. *IEEE Trans. Instrum. Meas.* **73**, 1–16 (2024).
7. Wang, Q., Lu, Y., Mishin, S., Oshmyansky, Y. & Horsley, D. A. Design, fabrication, and characterization of scandium aluminum nitride-based piezoelectric micromachined ultrasonic transducers. *J. Microelectromech. Syst.* **26**, 1132–1139 (2017).
8. Roy, K., Lee, J. E.-Y. & Lee, C. Thin-film PMUTs: a review of over 40 years of research. *Microsyst. Nanoeng.* **9**, 95 (2023).
9. Li, J. et al. A theoretical model of electromechanical coupling for CMUTs with annular electrodes based on the Ritz method. *Measurement* **246**, 116635 (2025).
10. Pan, J., Bai, C., Zheng, Q. & Xie, H. Review of piezoelectric micromachined ultrasonic transducers for rangefinders. *Micromachines* **14**, 374 (2023).
11. Xu, T. et al. Array design of piezoelectric micromachined ultrasonic transducers with low-crosstalk and high-emission performance. *IEEE Trans. Ultrason. Ferroelectr. Freq. Control* **67**, 789–800, https://doi.org/10.1109/TUFFC.2019.2956181 (2019).
12. Cheng, C. Y. et al. Thin film PZT-based PMUT arrays for deterministic particle manipulation. *IEEE Trans. Ultrason. Ferroelectr. Freq. Control* **66**, 1606–1615 (2019).
13. Gong, Y. et al. Ultrahigh-sensitivity coupled cantilever and dual-cavity piezoelectric micromachined ultrasonic transducers. *IEEE Electron Device Lett.* **45**, 897–900 (2024).
14. Wang, Z., Duan, H. & Zheng, Y. Multi-frequency broadband piezoelectric micromachined ultrasonic transducer utilizing Helmholtz resonance. *Int. J. Mech. Sci.* **249**, 108267 (2023).
15. Li, Z. et al. Pb (Zr 50 Ti 50) O 3-based piezoelectric micromachined ultrasonic transducers for high acoustic transmission and reception. *IEEE Electron Device Lett.* **45**, 1961–1964 (2024).
16. Zhao, L., Yang, C., Zhang, X., You, Z. & Lu, Y. Design, fabrication, and characterization of high-performance PMUT arrays based on potassium sodium niobate. *J. Microelectromech. Syst.* 1–8, https://doi.org/10.1109/JMEMS.2024.3395294 (2024)..
17. Sammoura, F. & Kim, S.-G. Theoretical modeling and equivalent electric circuit of a bimorph piezoelectric micromachined ultrasonic transducer. *IEEE Trans. Ultrason. Ferroelectr. Freq. Control* **59**, 990–998 (2012).
18. Smyth, K. & Kim, S.-G. Experiment and simulation validated analytical equivalent circuit model for piezoelectric micromachined ultrasonic transducers. *IEEE Trans. Ultrason. Ferroelectr. Freq. Control* **62**, 744–765 (2015).
19. Wang, Z. et al. Theoretical analysis and verification on ScAlN-based piezoelectric micromachined ultrasonic transducers with DC bias. *J. Microelectromech. Syst.* **33**, 54–65 (2023).
20. Li, Z. et al. Modeling and optimization of CMUTs arrays for improved transmission and reception performance in immersion. *IEEE Sens. J.* **24**, 7548–7563 (2024).
21. Akhbari, S., Sammoura, F. & Lin, L. Equivalent circuit models for large arrays of curved and flat piezoelectric micromachined ultrasonic transducers. *IEEE Trans. Ultrason. Ferroelectr. Freq. Control* **63**, 432–447 (2016).
22. Abdalla, O. M. O. et al. An experimental and numerical study of crosstalk effects in PMUT arrays. *IEEE Sens. J.* **23**, 29029–29041 (2023).
23. Zhao, L., Xia, J., Yang, C. & Lu, Y. Modeling and experimental studies of mutual acoustic radiation effect on PMUT array. *Sens. Actuators A Phys.* **377**, 115677 (2024).
24. Abdalla, O. M., Massimino, G., Savoia, A. S., Quaglia, F. & Corigliano, A. Efficient modeling and simulation of PMUT arrays in various ambients. *Micromachines* **13**, 962 (2022).
25. Sherman, C. H. & Butler, J. L. *Transducers and Arrays for Underwater Sound*. Vol. 4 (Springer, 2007).
26. Ventsel, E., Krauthammer, T. & Carrera, E. Thin plates and shells: theory, analysis, and applications. *Appl. Mech. Rev.* **55**, B72–B73 (2002).
27. Xu, T. et al. An analytical equivalent circuit model for optimization design of a broadband piezoelectric micromachined ultrasonic transducer with an annular diaphragm. *IEEE Trans. Ultrason. Ferroelectr. Freq. Control* **66**, 1760–1776 (2019).
28. Smyth, K., Bathurst, S., Sammoura, F. & Kim, S.-G. Analytic solution for N-electrode actuated piezoelectric disk with application to piezoelectric micromachined ultrasonic transducers. *IEEE Trans. Ultrason. Ferroelectr. Freq. Control* **60**, 1756–1767 (2013).
29. Sammoura, F., Smyth, K., Bathurst, S. & Kim, S.-G. in *2012 IEEE International Ultrasonics Symposium*. 580–583 (IEEE).
30. Liu, X. et al. Multiphysics modeling and analysis of Sc-doped AlN thin film based piezoelectric micromachined ultrasonic transducer by finite element method. *Micromachines* **14**, 1942 (2023).
31. Xu, T., Caponi, D. & Da, Z. in *2023 IEEE International Ultrasonics Symposium (IUS)*. 1–4 (IEEE).
32. Massimino, G., Colombo, A., Ardito, R., Quaglia, F. & Corigliano, A. Piezo-micro-ultrasound-transducers for air-coupled arrays: Modeling and experiments in the linear and non-linear regimes. *Extrem. Mech. Lett.* **40**, 100968 (2020).
33. Sarafianou, M. et al. Long-range high-resolution imaging with silicon-on-nothing ScAlN pMUTs. *IEEE Sens. J.* **23**, 24254–24263 (2023).
34. Zhou, J. et al. Continuous and non-invasive monitoring of blood pressure based on wearable piezoelectric micromachined ultrasonic transducers array. *J. Microelectromech. Syst.* **32**, 437–444 (2023).
35. Rosnitskiy, P. B., Vysokanov, B. A., Gavrilov, L. R., Sapozhnikov, O. A. & Khokhlova, V. A. Method for designing multielement fully populated random phased arrays for ultrasound surgery applications. *IEEE Trans. Ultrason. Ferroelectr. Freq. Control* **65**, 630–637 (2018).
36. Li, Z. et al. Highly-accurate and non-invasive flowrate monitoring for miniature pipelines using piezoelectric micromachined ultrasonic transducers. *Sens. Actuators A Phys.* **372**, 115339 (2024).
37. Zheng, Q. et al. Thin ceramic PZT dual-and multi-frequency pMUT arrays for photoacoustic imaging. *Microsyst. Nanoeng.* **8**, 122 (2022).
38. Wong, S. J., Roy, K., Lee, C. & Zhu, Y. Thin-film piezoelectric micromachined ultrasound transducers in biomedical applications: a review. *IEEE Transactions on Ultrasonics, Ferroelectrics, and Frequency Control* (2024).
39. Zhu, K. et al. Non-contact ultrasonic flow measurement for small pipes based on AlN piezoelectric micromachined ultrasonic transducer arrays. *J. Microelectromech. Syst.* **30**, 480–487 (2021).
40. Luo, G. et al. Small blind-area, high-accuracy ultrasonic rangefinder using a broadband multi-frequency piezoelectric micromachined ultrasonic transducer array. *Meas. Sci. Technol.* **34**, 125140 (2023).

41. Reddy, J. N. *Theory and Analysis of Elastic Plates and Shells* (CRC Press, 2006).
42. Vorländer, M. *Auralization: Fundamentals of Acoustics, Modelling, Simulation, Algorithms and Acoustic Virtual Reality* (Springer, 2008).
43. Porter, D. T. Self-and mutual-radiation impedance and beam patterns for flexural disks in a rigid plane. *J. Acoustical Soc. Am.* **36**, 1154–1161 (1964).
44. Chare, C. et al. Electromechanical equivalent circuit model for axisymmetric PMUTs with elastic boundary conditions. *J. Microelectromech. Syst.* **31**, 457–472 (2022).
45. Zhang, Y. et al. A low-voltage-driven MEMS ultrasonic phased-array transducer for fast 3D volumetric imaging. *Microsyst. Nanoeng.* **10**, 128 (2024).